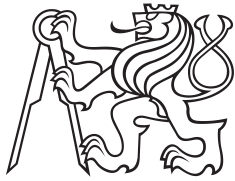


Master Thesis



Czech  
Technical  
University  
in Prague

**F4**

Faculty of Nuclear Sciences and Physical Engineering  
Department of Physics

# Simulation of electron beam transport within Hollow Electron Lens using Warp and Development of calibration method for Beam Loss Monitors

Bc. Sedláček Ondřej

Supervisor: Jiří Král Ph.D. (CTU-FNSPE)  
Supervisor–specialist: Adriana Rossi Ph.D. (CERN)  
August 2020

## Acknowledgements

I would like to acknowledge all the people that made this thesis possible, mainly my thanks go to my supervisor Jiří Král Ph.D. for his incredible patience with me and great help whenever it was needed. Next, I would like to greatly thank Adriana Rossi Ph.D., my CERN supervisor, for her guidance, providing numerous insights helping me advance with the project and kindly advising me on things that came along. Additionally, I would like to thank the people from beam loss and experimental area section as they were also very kind and helpful whenever it was needed. And also my appreciation goes to my father who always supported me during my studies as well as my friends which helped me to go through the whole process of which collage definitely is.

## Declaration

I declare that this work is all my own work and I have cited all sources I have used in the bibliography.

Prague, August 2020

Prohlašuji, že jsem svou diplomovou práci vypracoval samostatně a použil jsem pouze podklady (literaturu, projekty, SW atd...) uvedené v příloženém seznamu.

Nemám závažný důvod proti použití tohoto školního díla ve smyslu § 60 Zákona č. 121/2000 Sb., o právu autorském, o právech souvisejících s právem autorským a o změně některých zákonů (autorský zákon).

V Praze dne

Podpis:

## Abstract

The High Luminosity LHC aims to double the stored beam energy up to 700 MJ which challenges its collimation system and consequent beam losses measurements to new, greater performances. This thesis describes a proposed new stage of LHC collimation system, the Hollow Electron Lens (HEL) and a radiation-hard Diamond Beam Loss Monitors (dBLMs). The practical part of the work discusses relative calibration of the dBLMs response to LHC25ns like bunch train. A measurement was carried out to relatively calibrate the analog and digital chain of every dBLM at LHC in order to provide users with a rough measure of the relative beam losses. Calibration coefficients for the dBLM installations were calculated and readied for use in the control system. Further, a hollow electron beam was simulated in the first part of HEL using Warp code. The trajectory of the beam was found to be stable, with a beam offset of  $\approx 1.5$  mm after a bend, agreeing with the CST simulations. Mesh bending was studied and found to introduce no artifacts in the trajectory or the beam profile.

**Keywords:** High Luminosity LHC, Collimation system, Hollow electron lens, Warp, Diamond Beam Loss Monitors

**Supervisor:** Jiří Král Ph.D.  
(CTU-FNSPE)

## Abstrakt

High luminosity LHC upgrade plánuje zdvojnásobit uloženou energii ve svazku až na 700 MJ. Tento upgrade tedy klade zvýšené nároky na kolimační systém spolu s monitory měření ztrát svazku. Proto se tato práce zabývá radiačně odolnými diamantovými monitory ztrát svazku (dBLMs) a budoucí součástí kolimačního systému LHC dutou elektronovou čočkou (HEL). V praktické části je prezentována relativní kalibrace analogového a digitálního řetězce všech dBLMs v LHC pomocí měření výstupů dBLM na simulovaný LHC25ns bunch train signál. Z těchto výstupů následně byly vypočítány a implementovány kalibrační koeficienty do middleware kontrolního systému. Dále byla simulována evoluce dutého elektronového svazku v první polovině HEL pomocí Warp frameworku. Trajektorie systémem byla stabilní s pozorovaným propadem  $\approx 1.5$  mm za zahnutí systému. Tento propad byl také pozorován a v dobré shodě se simulacemi z CST simulačního programu. Efekty způsobené zahnutím simulační mřížky byly studovány avšak žádné artefakty nebyly nalezeny v trajektorii či profilu svazku.

**Klíčová slova:** High Luminosity LHC, Kolimační systém, Dutá elektronová čočka, Warp, Diamantové monitory ztrát svazku

**Překlad názvu:** Simulace transportu elektronového svazku dutou elektronovou čočkou pomocí programu Warp a vývoj kalibrační metody pro detektory ztrát svazku

# Contents

<b>1 Theoretical Part</b>	<b>1</b>
1.1 LHC time plan .....	1
1.2 Collimation system at LHC/Collimators .....	3
1.2.1 Hollow electron lens .....	5
1.3 Beam loss monitors .....	9
1.3.1 Diamond Beam Loss Monitors at LHC .....	12
1.4 Simulation of high current electron beam.....	15
1.4.1 Warp Code Framework for Kinetic Simulations of Particle Beams and Plasmas.....	16
<b>2 Practical part</b>	<b>21</b>
2.1 Calibration of Diamond Beam Loss Monitors .....	21
2.1.1 Response measurement .....	22
2.1.2 Analysis .....	23
2.1.3 Results .....	25
2.2 Warp simulations of Hollow Electron Lens .....	27
2.2.1 General simulation setup....	28
2.2.2 Magnetic field .....	30
2.2.3 Conductor construction .....	31
2.2.4 Diagnostics.....	33
2.2.5 Results .....	34
<b>3 Discussion</b>	<b>43</b>
<b>4 Conclusions</b>	<b>45</b>
<b>A Bibliography</b>	<b>46</b>
<b>B Warp simulation file</b>	<b>49</b>
<b>C Warp configure file</b>	<b>59</b>

## Figures

<p>1.1 The CERN Accelerator complex scheme including several experiments and experimental areas. . . . . 1</p> <p>1.2 Upgrade program of LHC including High Luminosity upgrade and past stages. . . . . 2</p> <p>1.3 Beam core and beam halo (beam tails) illustration for a Gaussian distribution of a beam (red line). Overpopulated tails can be intercepted by collimator jaws (black blocks). . . . . 3</p> <p>1.4 Illustration of a multistage collimation system, with primary collimator (black) and a set of secondary collimators (grey) jaws. . . 4</p> <p>1.5 A map of the LHC collimation system [7]. . . . . 5</p> <p>1.6 Illustration of a LHC multistage collimation system with the description of various collimation stages [7]. . . . . 6</p> <p>1.7 A 3D model of the Hollow Electron Lens design [9]. . . . . 6</p> <p>1.8 Transverse view of a hollow electron beam (orange) and proton beam core (blue) [10]. . . . . 7</p> <p>1.9 A current 3D model of an electron gun of the Hollow Electron Lens [9]. 7</p> <p>1.10 Placement of the Hollow Electron Lens in the multistage collimation system [11]. . . . . 8</p> <p>1.11 Up, a transverse view of the beams in Tevatron pipe including hollow electron, proton, and anti-proton beam is shown. Down, a design of the electron lens at Tevatron used in the hollow beam scrapping studies is shown [13]. . . . . 9</p> <p>1.12 Inside structure of a ionization chamber a) and an example of a mounted chambers (yellow tubes) at CERN around a quadrupole magnet (white part of the pipe). [17] . . . . . 12</p>	<p>1.13 A two face-to-face PIN diodes detecting in coincidence to suppress the low energy photons from synchrotron radiation a) and a Secondary emission detector b). [19, 22] . . . . . 12</p> <p>1.14 Diamond particle detector and analog chain of a diamond beam loss monitor structure at LHC. . . . . 13</p> <p>1.15 Illustration of beam trajectories during beam dump kicker magnet (MKD) rise time [24]. . . . . 15</p> <p>1.16 Scheme of linear weighting using are in 2-dimensional simulations. Areas <math>a, b, c, d</math> are used as weights (after normalization) corresponding to the grid point <math>A, B, C, D</math>, respectively. [29]. . . . . 17</p> <p>1.17 Time evolution of leap-frog algorithm [29]. . . . . 19</p> <p>1.18 a) Illustration of a mesh in warped Cartesian Frenet–Serret coordinates. b) Illustration of different sets of coordinates in the bend [36]. . . . . 20</p> <p>2.1 A scheme of relative diamond beam loss calibration. . . . . 22</p> <p>2.2 A scheme of diamond beam loss monitor response measurement. . . . . 22</p> <p>2.3 An example of the input train waveform (8 out of 10 signals shown). The configured signal parameters are noted, including separation between signal peaks, positive and negative edge and total signal duration. An amplitude is shown, however it changed from system to system. . . 23</p> <p>2.4 Measured output data of ua23 TDI channel 1 to train a), single waveform b) and ua23 TCDI channel 0 to train c), single waveform d). The setup parameters can be found in Table 2.1 . . . . . 26</p>
--	--

2.5 Longitudinal view of the simulated geometry with key parameters included. Conductors (black) are according to Hollow Electron Lens design. The electron gun is scaled design of V. Moens [38]. . . . .	27	2.13 Longitudinal view of a beam trajectory with magnetic field lines in Cartesian a) and Warped b) coordinates. The potential on the cathode was to -15kV, on anode -5kV, and pipe was grounded. . . . .	35
2.6 Longitudinal view of the electron gun geometry with a magnitude of the electrostatic field shown with -15kV on the cathode (and control electrodes), -5kV on the anode and grounded pipe. Conductors (green) are according to the scaled-down design of Vince Moens 1-in electron gun [38] to 0.634-in electron gun. The compression of the extracted beam (purple) is caused by a magnetic field. . . . .	29	2.14 The calculated magnetic self-field in the beam at $x = 0$ mm and $z = 0.125$ m a), $z = 0.360$ m b), $z = 0.415$ m c), $z = 0.525$ m d). The applied magnetic field is 0.37 T at gun and $\approx 5$ T at the main solenoid. 36	36
2.7 Longitudinal view of the mesh (blue) and conductors (black) of the simulations. . . . .	30	2.15 Longitudinal view of a beam trajectories for different evolution times in a laboratory frame parallel with proton pipe. Overall view a) zoomed section after bend b). The potential on the cathode was -15kV, on anode -5kV and pipe was grounded. . . . .	38
2.8 Longitudinal view of the mesh center-lines used in the bend effect study to probe the effect of the bent mesh on the particle trajectory and profile cross section. Each center-line represents one mesh (i.e. the blue line represent the blue column in Figure 2.7) and for each mesh one simulations was carried out. . . . .	31	2.16 The average vertical beam position of a beam trajectories for different evolution times in a laboratory frame parallel with proton pipe. Overall view a) zoomed section after bend b). The spread for different evolution times is $\sigma = 37$ $\mu$ m. The potential on the cathode was -15kV, on anode -5kV and pipe was grounded. . . . .	39
2.9 Magnitude of magnetic field extracted from CST and used in the Warp simulations. . . . .	32	2.17 Current a) and Energy b) along the longitudinal warped coordinate for different anode potentials. Additionally, a current calculated from Child-Langmuir law (black) is shown for reference. . . . .	39
2.10 Hollow Electron Lens design as modeled in CST. Courtesy of Antti Kolehmainen and Diego Perini, CERN. . . . .	33	2.18 Beam offset behavior to varying beam current and energy and comparison to CST simulations (black). The trajectories spread for different current is $\sigma = 28$ $\mu$ m. The errors presented are taken from time-stability study shown above and represent accuracy of the simulations. . . . .	40
2.11 Injection (black), junction (red) and proton (green) pipe design to illustrate the junction construction. 33	33		
2.12 Longitudinal view of the beam with its energy color-coded. The potential set on the cathode was to -15kV, -5kV on anode and pipe was grounded. . . . .	34		

2.19	Longitudinal view of a beam trajectory in a laboratory frame parallel with electron pipe. Overall view a) zoomed section of the virtual cathode b). The potential on the cathode was -10kV and anode was grounded as well as the pipe. . . . .	41
2.20	Longitudinal view of a beam trajectories of simulations with different bending radii of meshes in a laboratory frame parallel with electron pipe. Overall view a) zoomed section after the bend b). . .	41
2.21	Beam offset of a beam trajectories of simulations with different bending radii of meshes. Overall view a) zoomed section of the virtual cathode b). The trajectories spread for different current is $\sigma = 21 \mu\text{m}$ . . . .	42
2.22	Beam profile of a beam trajectories of simulations with different bending radii of meshes after the bend at $z=-1.655\text{m}$ in laboratory frame parallel with electron pipe. Slight asymmetries are visible; however, no observed artifact caused by different mesh bending radii. . .	42

## Tables

1.1	The type, location, abbreviation and number of collimators in LHC collimation system [7]. . . . .	7
1.2	The locations of diamond beam loss monitor situated at LHC, their associated accelerator component (Abbreviations summarized at Table 1.1) and area of beam loss measurement. . . . .	14
2.1	Summary of the relative calibration's input parameters and average integrals of the raw output data and calculated calibration coefficients. Each Diamond Beam Loss Monitor is characterized by the detector and <i>Electronic</i> location and connected <i>Channel</i> (Ch). The generator & circuit set up parameters are: <i>Attenuation</i> (Att) at signal generator and input signal peak to peak <i>Amplitude</i> (In Ampt) of the generator. The signal input is described in subsection 2.1.1. The outputs and results are described by resulting average <i>Output integral</i> for train signal and calculated <i>Calibration coefficient</i> . . . . .	25

# Chapter 1

## Theoretical Part

### 1.1 LHC time plan

CERN, the European Organization for Nuclear Research, hosts a large accelerator complex depicted in Figure 1.1 with its crown jewel the Large Hadron Collider (LHC).

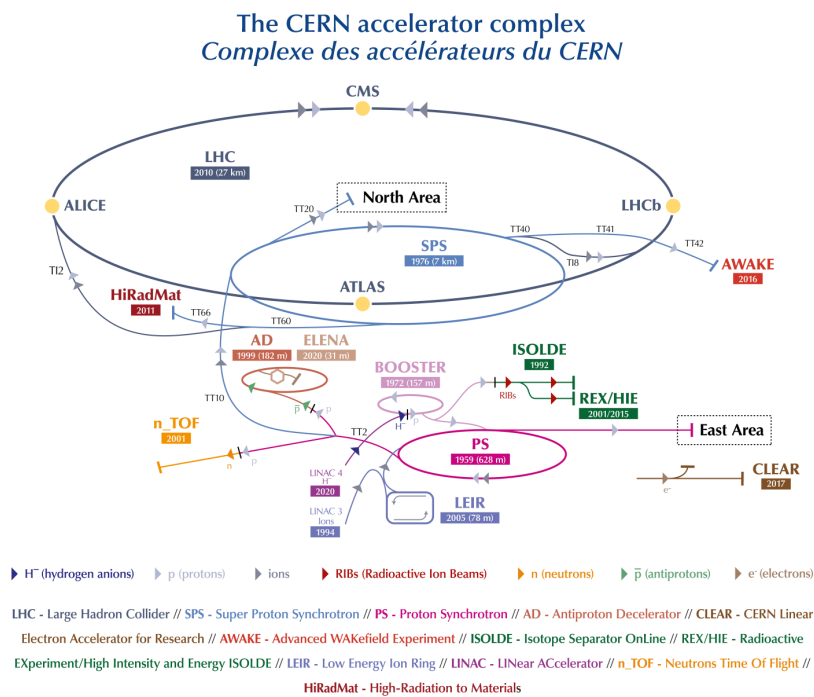


**Figure 1.1:** The CERN Accelerator complex scheme including several experiments and experimental areas [1].

The accelerator complex keeps evolving to advance its research and other capabilities. Therefore every several years the complex undergoes a multi-year long shutdown (LS) that presents a possibility for a minor or major upgrades. Figure 1.2 outlines the LHC road map. In 2014-2015 during LS1 the center

of mass energy reached at LHC was upgraded from 7-8 TeV to 13 TeV and bunch spacing decreased from 50ns to 25ns [2]. Currently, in 2019 and 2020, CERN is in LS2, upgrading the central mass energy to 14 TeV and doubling the nominal luminosity for Run 3 [3].

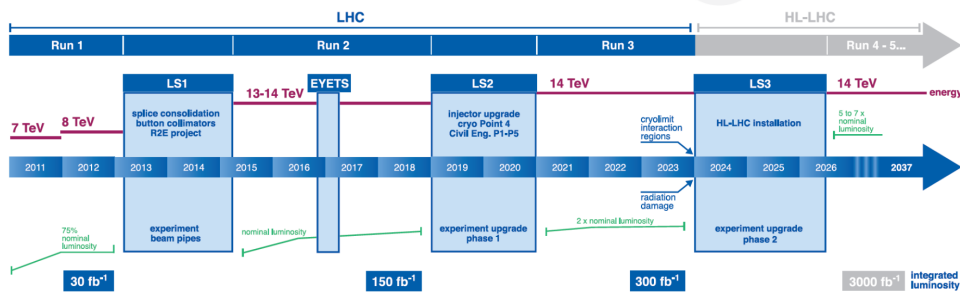


**Figure 1.2:** Upgrade program of LHC including High Luminosity upgrade and past stages [4].

The next planned long shutdown is LS3 starting in 2024 also called High-Luminosity LHC upgrade (HL-LHC). This upgrade is supported by European Strategy for particle physics - Update 2013 as well as in the recent update in 2019. The HL-LHC keeps the central mass energy at 14 TeV, however, plans to double yet again the luminosity to approximately 5 times of the design value [3].

The raised luminosity brings many benefits to experiments such as larger chances of observing rare events or increased precision of other studies which both can lead to a discovery of new physics or improving the precision of the original results.

The HL-LHC is an ambitious project for which many limitations must be overcome and new technologies employed. The beam stored energy will be raised up to 700 MJ surpassing the current radiation damage limit which is 350 MJ (expected to be reached after LS2). The collimation system, that protects the machine from excessive beam losses must be, therefore, substantially upgraded. Several projects are foreseen, such as replacing a standard 8.33 T main dipoles magnets with two shorter 11 T dipoles with an additional collimator between them [5] or deployment of Hollow Electron Lens (HEL).

The topic of this thesis focuses on HEL and Diamond Beam Loss Monitors (dBLMs) both of which are important parts for a collimation system upgrade. The HEL is a new advanced system for active control of beam particles diffusion speed discussed which is foreseen to be installed in LS3 [6]. And the dBLMs are measuring and studying the intense beam losses mainly in the vicinity of collimators. The practical part of this work presents numerical simulations of a HEL beam together with the relative calibration of an analog and digital chain of every dBLMs at LHC.

## 1.2 Collimation system at LHC/Collimators

A Collimation system is increasingly important with the rising energy of the stored beam in modern colliders. For reference, the design beam stored energy in LHC is 362 MJ, and in the High Luminosity upgrade even 700 MJ. This makes the beam highly destructive when not controlled and collimated properly [7]. Additionally, the beam can quench a superconducting magnet by depositing as little as  $30 \text{ mJ/cm}^{-3}$  corresponding to  $4 \cdot 10^7$  protons at 7 TeV while  $\approx 10^{13}$ - $10^{14}$  protons are present in a single typical LHC bunch [8]. Therefore, the collimation system must evolve with the colliders as higher energies and intensities are achieved to protect the machines.

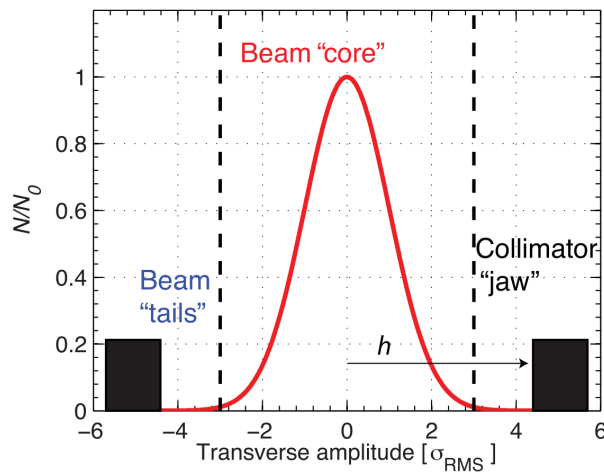


**Figure 1.3:** Beam core and beam halo (beam tails) illustration for a Gaussian distribution of a beam (red line). Overpopulated tails can be intercepted by collimator jaws (black blocks) [7].

**Roles of Collimators.** There are several important roles of a collimation system. Firstly, it cleans a beam halo during a collider operation, such that the beam-induced quenches of the superconducting magnets are avoided [8]. Beam halo is usually defined as particles with transverse amplitudes (or energy deviations) significantly larger than the beam core. Assuming Gaussian distribution of the beam, which is typically an adequate model for the beam core, one often uses  $3\sigma$  as the difference between beam core and beam halo (or beam tails) as shown in Figure 1.3. Another effect of the halo cleaning is lowering a background noise to the experiments, originated by halo particles lost in the experimental detector.

Secondly, a collimation system provides passive protection for the machine. Collimators regions represent the closest elements to the beam, therefore, acting as a first defense line against expected or unexpected beam losses. Consequently, the collimators act also as a radiation dose dumps concentrating radiation load on them and reducing it on the rest of the machine [7]. Beam losses are detected by Beam Loss Monitors (BLMs) situated close to the

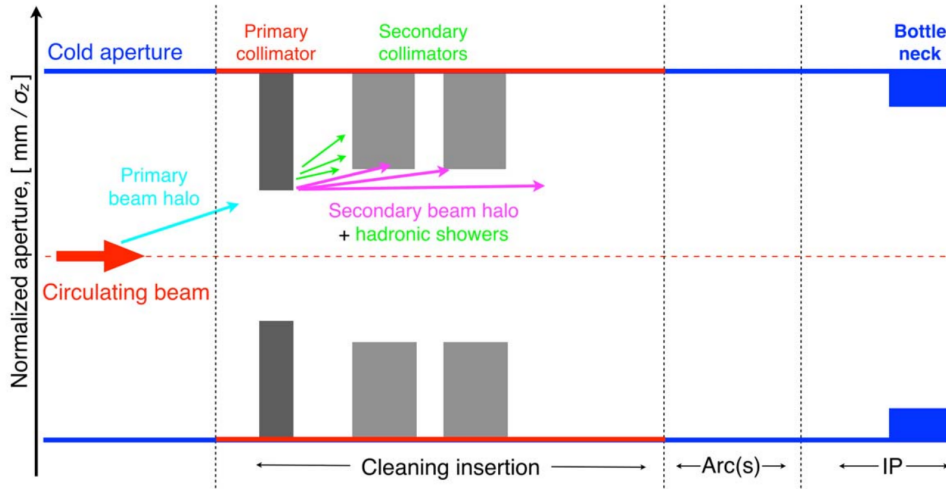


**Figure 1.4:** Illustration of a multistage collimation system, with primary collimator (black) and a set of secondary collimators (grey) jaws [7].

collimators described in section 1.3.

During dedicated experiments, collimators can also be used to indirectly measure the halo population by moving their jaws progressively across the beam (beam scraping), and measuring losses at the BLMs [8].

**Multistage collimation system.** A working principle of a collimator is absorbing beam particles by moving a collimation jaws (blocks with graphite and metal (tungsten or copper) inserts) into the particle trajectories as shown in Figures 1.3 and 1.4. The interaction of halo particles with the jaws of a primary collimator (TCP) creates secondary particles (and hadronic shower); therefore, it is necessary to use secondary collimators (TCS) to intercept this secondary beam halo. Such a collimation system using more than the primary collimator is called multi-stage and is illustrated in Figure 1.4. The total length of secondary collimators is typically larger to absorb the particles out-scattered by TCPs. At the same time, their aperture is larger to keep the collimator hierarchy and avoiding the creation of a new secondary halo particles [7].

**LHC collimation system.** The LHC collimation system, shown in Figure 1.5, achieves better performance than the the multistage system described above by adding more "stages" as depicted in Figure 1.6. In particular a shower absorber<sup>1</sup> after secondary collimators to absorb hadronic showers, and tertiary collimators to intercept the beam scattered halo and showers produced at the secondary collimators [7].

Most of the collimators (primary and secondary collimators) are located in the cleaning regions, IR7 and IR3 as shown in Figure 1.5 and summarized in Table 1.1.

<sup>1</sup>Absorber is a round thick element usually made of high Z material, like Tungsten, mounted around the vacuum chamber.

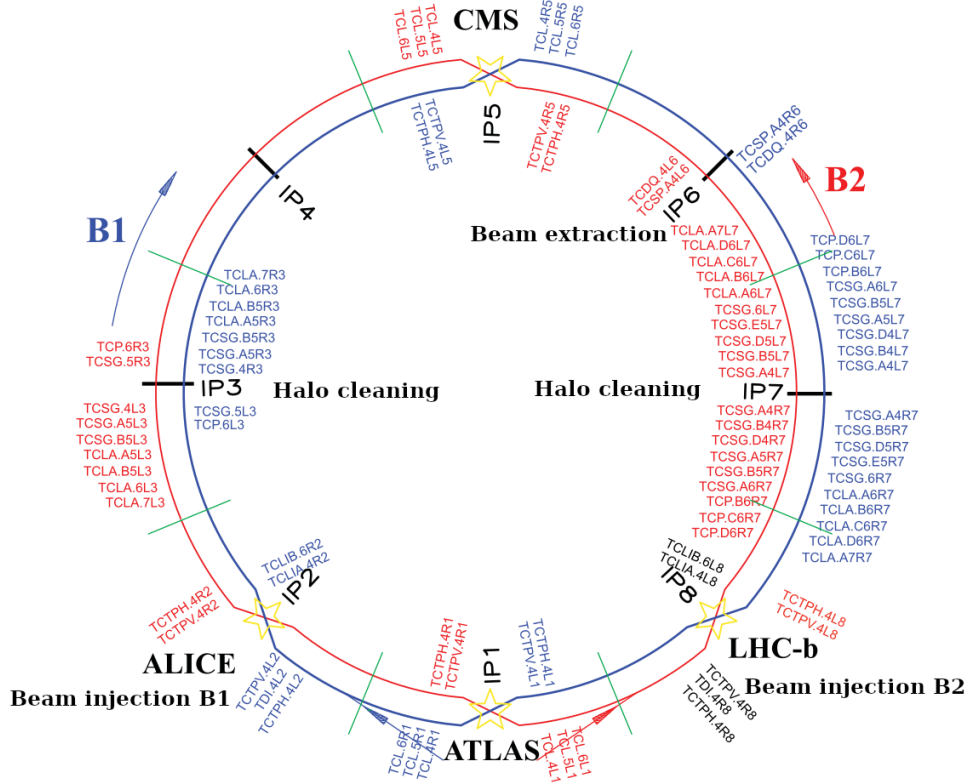


Figure 1.5: A map of the LHC collimation system [7].

Tertiary collimators are installed before critical bottlenecks (inner triplet magnets), installed on both sides of the experiments in regions IR1,2,5 and 8.

In dump regions protection devices shields the machine in case of kicker failure [7].

Before and after the experiments in regions IR1,2,5 and 8 the beam is additionally cleaned using tertiary collimators and absorbers. Beam injection is located in regions IR2,8 and extraction in IR6 both shielded by dedicated collimators and protection devices [8, 7].

### 1.2.1 Hollow electron lens

The Hollow Electron Lens (HEL) aims to improve the collimation performance by active control of beam halo diffusion speed as a part of the High-Luminosity upgrade of LHC [11]. As noted earlier the upgrade plans to almost double the beam current, with a corresponding the beam stored energy reaching 700 MJ. According to dedicated studies [12, 6], the beam tails are overpopulated with respect to normal Gaussian distribution and the energy stored in the beam tails is estimated to be 30 MJ. Therefore, the collimation system must be properly adjusted. There are also several other projects focusing on improving the collimation system, for example, addition of 15-20 new and replacement of 60 already existing collimators or crystal collimators [5].

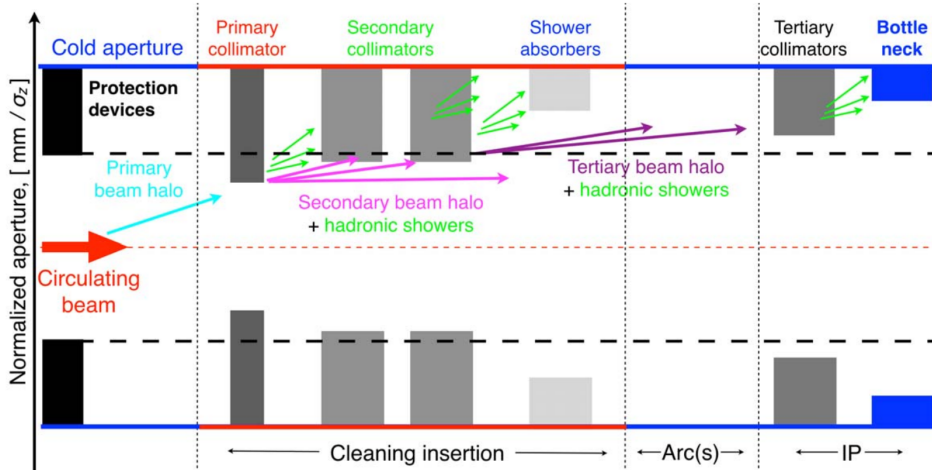


**Figure 1.6:** Illustration of a LHC multistage collimation system with the description of various collimation stages [7].

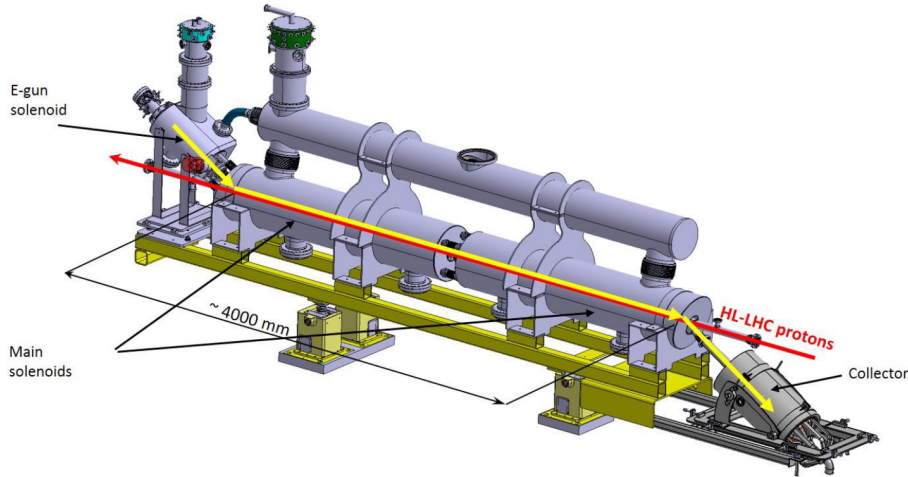


**Figure 1.7:** A 3D model of the Hollow Electron Lens design [9].

HEL is a system emitting and magnetically guiding a hollow low-energy, high-current electron beam into the LHC beam pipe in a way that only the tails of the proton or ion beam travelling through the hollow electron beam interact with the electrons. After  $\approx 3$  m of parallel trajectory, the electron beam is guided out and extracted. A 3D model of the HEL is shown in Figure 1.7. The halo of the proton beam receives tunable non-linear transverse kicks from the electron beam while the core should be unaffected in the hollow center as displayed in Figure 1.8 [10]. The system should be incorporated into the collimation at apertures smaller than the TCP gap to kick the beam losses into the primary collimator as detailed in Figure 1.10 [11].

Type	Locations	Abbreviation	Number
Primary	IR3,7	TCP	8
Secondary	IR3,7	TCSG	30
Absorbers	IR3,7	TCLA	18
Tertiary	IR1,2,5,8	TCTP	16
Dump protection	IR6	TCSP,TCDQ	4
Injection protection (lines)	TI2,8	TCDI	13
Injection protection (ring)	IR2,8	TDI,...	7

**Table 1.1:** The type, location, abbreviation and number of collimators in LHC collimation system [7].

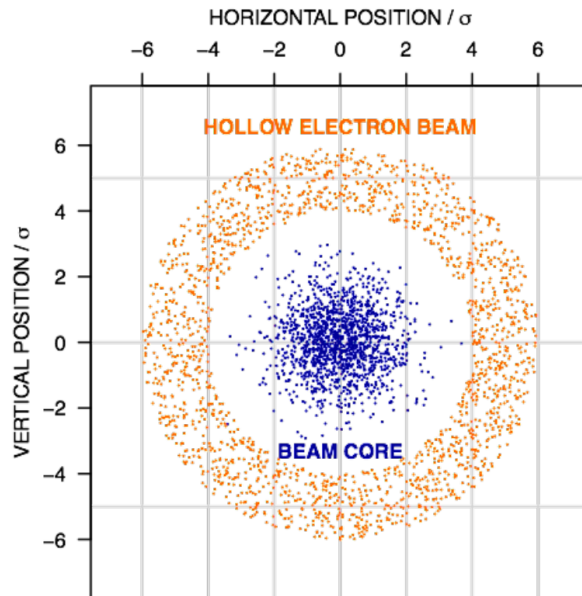


**Figure 1.8:** Transverse view of a hollow electron beam (orange) and proton beam core (blue) [10].

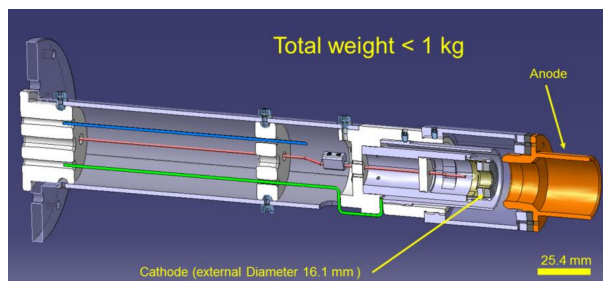


**Figure 1.9:** A current 3D model of an electron gun of the Hollow Electron Lens [9].

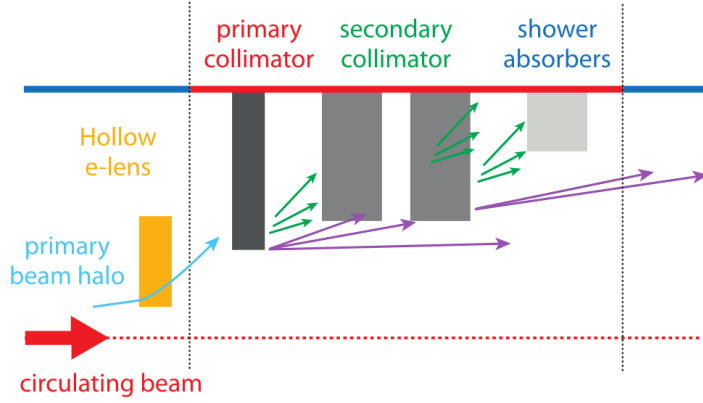


**Figure 1.10:** Placement of the Hollow Electron Lens in the multistage collimation system [11].

**Hollow electron lens structure.** The Hollow Electron Lens can be divided into several parts: thermo-ionic electron gun embedded into a gun solenoid, bend solenoid, main solenoid, a second bend solenoid and collector as can be seen in Figure 1.7. The electron gun, shown in Figure 1.9, emits a hollow electron beam of a current approximately 5.2 A with 10 kV difference between anode and cathode. The beam is accelerated to 15 keV since the difference in potential between the cathode and the vacuum pipe - grounded - is of 15 kV. The cathode has an outer diameter of 16.1 mm and an inner diameter of 8.05 mm and the working temperature is 950 deg C.

The electron gun is immersed in a solenoid magnetic field of  $\approx 0.37$  T; therefore, the beam is magnetized and guided by the magnetic field lines [9]. The beam is then guided and bent into the proton pipe with the main solenoid where the magnetic field is  $\approx 5$  T leading to a compression according to the formula:

$$\frac{r_{gun}}{r_{main}} = \sqrt{\frac{B_{main}}{B_{gun}}} \approx 3.67 \quad (1.1)$$

Where  $r_{gun}$ ,  $B_{gun}$ ,  $r_{main}$  and  $B_{main}$  is a radius of the beam and magnetic field in the gun and main solenoid, respectively. As can be seen, the beam radius in the proton pipe is tunable by only varying the magnetic field in the gun solenoid. This is especially useful since it allows to vary the beam radius while keeping a constant magnetic field in the main solenoid.

The beam is transported through two main solenoids and then guided out of the LHC beam pipe and into the collector.

**Electron lens in Fermilab.** Two electron lenses were installed at Tevatron collider and used for long-range and head-on beam-beam compensation and abort gap cleaning [6]. Studies of hollow beam scrapping were carried out [14, 13, 15]. In these studies, a pulsed 5 keV hollow electron beam was transported with a strong axial field through a design shown in Figure 1.11.

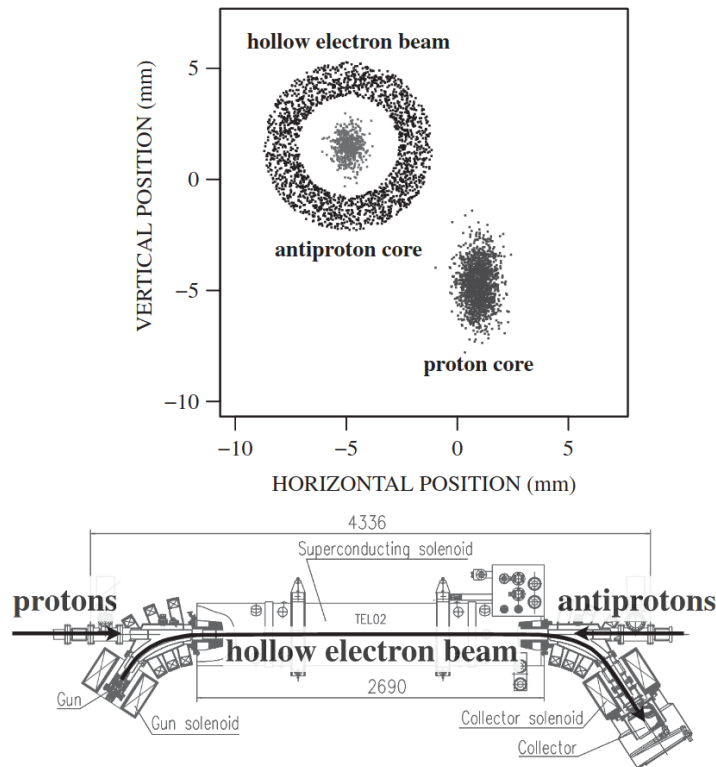


**Figure 1.11:** Up, a transverse view of the beams in Tevatron pipe including hollow electron, proton, and anti-proton beam is shown. Down, a design of the electron lens at Tevatron used in the hollow beam scrapping studies is shown [13].

The results of these studies suggest that such a system can act as a tunable diffusion enhancer extending the conventional collimation system beyond the intensity limits imposed by tolerable losses [13, 15].

## 1.3 Beam loss monitors

Beam loss monitors (BLMs) provide information about beam losses via measuring the secondary particle showers. Beam losses are particles which fall out of the stable beam phase space. The showers are then result of the lost beam particle interacting with materials in their path, mainly vacuum chamber walls and magnets[16].

The BLM typical structure is a detector, measuring the showers, followed by an analog and digital chain, processing the signal and establishing the beam losses at a certain position and within a specified time interval [16].

The number of detected particles and the signal output from the BLM should be proportional to the beam losses. However, this proportionality depends on the experimental setup. For example, the position of the detector with respect to the beam, the type of lost particles or the material they traveled through are affecting the proportionality. Moreover, the proportionality

depends on the momentum of the lost particles, which may greatly vary during the acceleration cycle [16].

**Beam losses.** Beam losses can be caused by many different known or unknown mechanisms. This means, that the beam losses can have very different characteristics. One can distinguish two classes of beam losses: [17, 18]:

- Irregular losses – Losses that are not expected, usually not repeating, and having high intensity in a short time window. The reason is often a beam misalignment or a fault condition such as a trip of the HF-system, magnet supply or other [17].
- Regular Losses – Losses caused by known mechanisms, usually characterized by having lower intensity and repeated patterns. These losses are typically unavoidable and localized on the collimator system or other (hopefully known) aperture limits such as quadrupole magnets. [18].

**Beam loss monitor uses.** There are three main uses for the BLM system in particle accelerators [16]:

- Accelerator and detector protection – High and frequent irregular losses can activate or greatly damage the accelerator or nearby detectors. Moreover, heat deposition in superconducting magnets caused by the beam loss can result in magnet quench. By measuring beam losses, the BLM system can identify a disrupted beam and request a dump before more or any damage is caused. This is essential in preventing damage, but also, lower activation, as necessary for hands-on maintenance [18].
- Accelerator setup and diagnostics – Obstructions in the beam path create large irregular beam losses. Therefore, measuring the position of the beam loss in combination with its magnitude is a very effective way of obstruction localization. On the other hand, the BLMs are used for setup and control of the collimating system and tuning the injection by measuring the regular beam losses around the collimators and injection points [17].
- Improve accelerator performance – Several unavoidable effects can limit the beam lifetime, and therefore, accelerator performance. One example can be the Touschek effect, where bunched particles performing transverse oscillations can scatter increasing their longitudinal momenta, and falling (in phase-space) outside the bunch bucket. In this case, the two colliding particles lose and gain an equal amount of momentum, therefore, one hit the inside and other outside of the vacuum chamber. Measuring the beam losses at these locations in coincidence can, therefore, help to understand and limit this effect [18].

Obviously, it is advantageous to use a BLM system covering all beam losses, therefore functioning over a very large dynamic range [17, 16].

**Beam loss monitors types.** Different types of BLM are characterized by the particle detector used. Several examples are:

- Ionization chambers – Long or short ionization chambers are tubes filled typically with argon or nitrogen where the secondary particles interact and create electron-ion pairs. These pairs are then collected by a series of high-voltage gaps along the length of the chamber. The resulting current is measured and results to be proportional to the beam loss. Figure 1.12 shows a typical assembly configuration at CERN-LHC. This type of BLM is often used because it provides good sensitive volume, is radiation hard, reliable [17, 16].
- PIN Photodiodes – PIN (positive-intrinsic-negative) diodes are semiconductor devices that act essentially as solid state ionization chambers. The particles passing through the sensitive volume creates electron-hole pairs that are collected at biased plates. The advantage is that they are very fast and with some semiconductors, e.g. diamond, also highly radiation hard and with a high dynamic range. Diamond beam loss detectors are relatively new, and are used mainly for beam studies for example at LHC or SPS in high-radiation environments. A set of two face-to-face PIN diodes, shown in Figure 1.13 a), working in coincidence is used to suppress the low energy photons from synchrotron radiation. Due to the low penetration depth, these photons are typically absorbed in one diode and do not reach the other diode. On the other hand, higher energy charged particles created by other means penetrate both diodes. These devices are useful especially at electron hadron accelerators such as HERA. The downside of PIN diodes is its small sensitive volume and, therefore, a rather low detection efficiency [19, 20, 17].
- Scintillation detectors – Scintillation detectors use a fluorescent effect<sup>2</sup> to detect particles. The typical Scintillation detector consists of a scintillation material emitting light as a response to particle passing through, the photo-multiplier converting the light into electrons which are subsequently multiplied and signal readout. The Scintillators are usually dissolved in plastic or liquid and can, therefore, take arbitrary shape, are fast and quite cheap to make. On the other hand, a big disadvantage is low radiation hardness. For that reason, the scintillation detectors are often used as a temporary Beam Loss Monitors or at lower radiation environment [16, 20].
- Secondary Emission monitor – The secondary emission monitors exploit the secondary emission from a surface caused by particles traveling through it. An illustration photo can be seen in Figure 1.13 b) Their

<sup>2</sup>The fluorescence refers to the emission of light by de-excitation of a molecule or an atom as a response to excitation. A Phosphorescence is closely related and differs in the de-excitation cascade and wavelength of emitted light. In practical fluorescence is fast  $\approx 10\text{ns}$  and phosphorescence slow, typically,  $> 10^{-3}\text{s}$  and undesirable for scintillation detectors. More in [21]

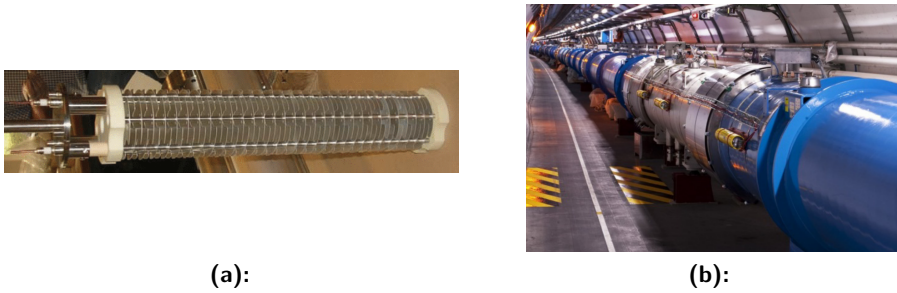


**Figure 1.12:** Inside structure of a ionization chamber a) and an example of a mounted chambers (yellow tubes) at CERN around a quadrupole magnet (white part of the pipe). [17]

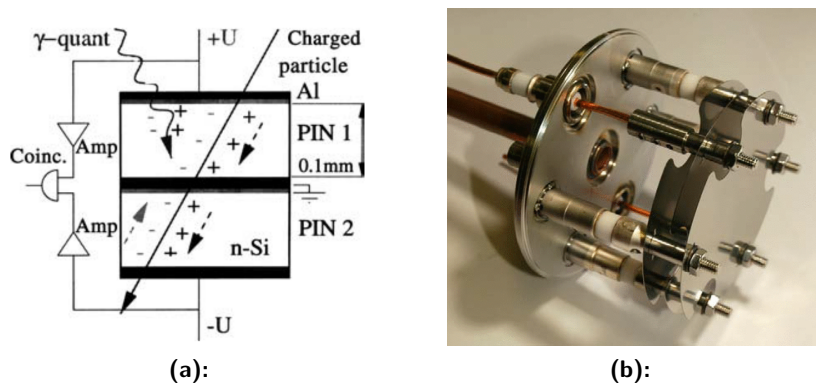


**Figure 1.13:** A two face-to-face PIN diodes detecting in coincidence to suppress the low energy photons from synchrotron radiation a) and a Secondary emission detector b). [19, 22]

sensitivity is quite low, but the radiation hardness is very high. Therefore, it makes sense to put them into high radiation areas (e.g. at LHC around collimators) where other detectors would be saturated or damaged [20, 16].

### 1.3.1 Diamond Beam Loss Monitors at LHC

The energy stored at LHC during operation is  $\approx 350$  MJ, but energy deposition of only a few  $\text{mJ}/\text{cm}^3$  is enough to quench a superconducting magnet [? ]. Approximately 4000 ionization chamber Beam Loss Monitors are installed around the LHC to detect beam losses and dump the beam whenever necessary [23]. The ionization chamber BLMs provide time resolution of  $\approx 40 \mu\text{s}$ , however, a time resolution better than bunch spacing  $\approx 25$  ns is crucial in understanding the beam loss mechanism [24]. For that reason, 14 Diamond Beam Loss Monitors are installed at LHC providing time resolution of  $\approx 1$  ns allowing to study the beam losses on a bunch-by-bunch basis.

### ■ Diamond beam loss monitor structure

Diamond BLM at LHC uses in most cases a poly-crystalline particle diamond detector. The signal output of the detector is connected to a AC/DC splitter, where the AC part of the signal is typically amplified by a current amplifier with bandwidth of 2GHz. The detector system is mounted on a metal panel usually above the beam pipe as shown in Figure 1.14 and a coaxial cable typically about  $\approx 200\text{m}$  long connects to the read-out system [25]. The data are then digitized by analog to digital converter (ADC) and processed by the acquisition system containing an FPGA.

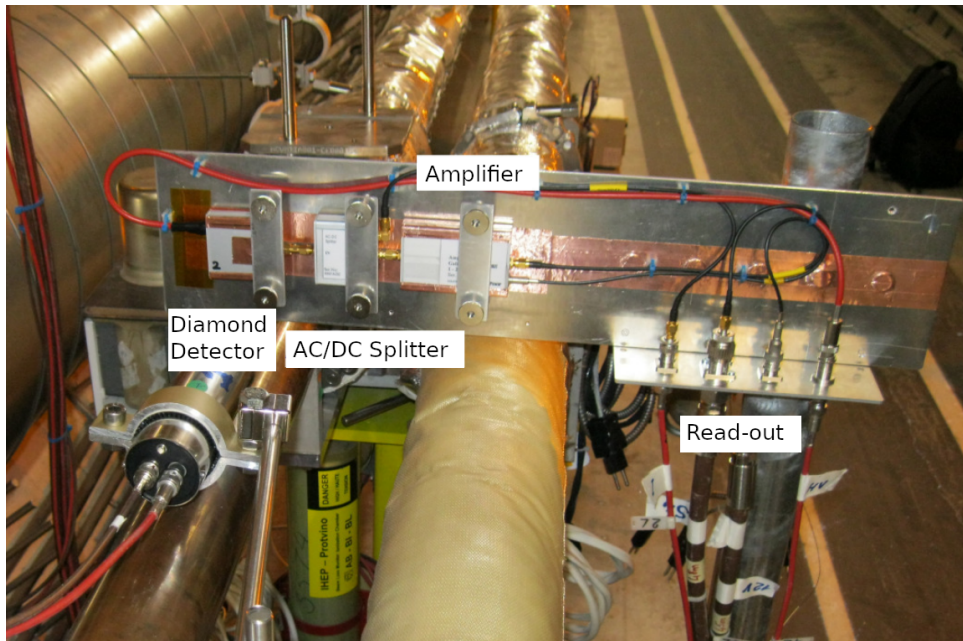


**Figure 1.14:** Diamond particle detector and analog chain of a diamond beam loss monitor structure at LHC.

### ■ Diamond beam loss monitor usage at LHC

Fourteen diamond BLMs are installed at various areas along LHC including injection, beam cleaning, beam dump and a position with history of higher beam losses. Additional four diamond BLMs are situated at the collimation area in the injection transfer lines. Table 1.2 summarizes position and other information of each monitors.

*Beam injection.* Two diamond BLMs are installed at IR2 and IR8 downstream of the internal beam absorber blocks for injection losses (TDIs) to study the beam losses during injection for example caused by injection oscillations [24].

In 2015 the nanosecond time resolution of the installed dBLMs at injection allowed identification of recaptured SPS beam as a major contributor to the

Location Electronics	Monitor	Associated component	Number of monitors	Measurement area
ua23	IR2	TDI	2	Beam injection
ua23	TI2	TCDI	2	Transfer line collimation
ua23	IR3	-	2	Position with high beam loss history
ua87	IR8	TDI	2	Beam injection
ua87	TI8	TCDI	2	Transfer line collimation
us65	IR6	TCDQ	2	Beam dump
ua76	IR7	TCP	4	Beam cleaning
tz76	IR7	TCHS	2	Beam cleaning

**Table 1.2:** The locations of diamond beam loss monitor situated at LHC, their associated accelerator component (Abbreviations summarized at Table 1.1) and area of beam loss measurement.

beam losses. After tuning the injection, the losses were reduced by 60%. More in [26].

*The transfer line collimation.* Two diamond BLMs are installed at TI2 and TI8 transfer line collimators (TCDIs) to study the beam losses during transfer line collimation.

*Beam dump.* Two diamond BLMs (one per beam) are installed at IR6 next to the movable dump protection absorber (TCDQ) to derive the number of nominal bunches impacting the TCDQ.

The dBLMs are necessary for their time resolution, but also because in case of an asynchronous beam dump with fully filled LHC machine it is expected that all standard ionization chamber BLMs in the region will be saturated [27].

*Beam cleaning.* Four diamond BLMs (two per beam) are installed near the primary collimators (TCP) and additional two dBLMs (one per beam) near the Target Collimator Halo Scraper (TCHS) at IR7 to study beam losses during betatron collimation. The main goal of dBLM at this area is to measure beam losses for further understanding of beam dynamics in the LHC and optimizing its operation [28, 25].

This area is very potent for beam loss study because several beam loss mechanisms can be studied here (e.g. beam losses caused by UFOs, instabilities, etc.). Also, beam losses during beam dump caused by the rise time of the beam dump kicker magnets are measurable at TCDQ at IR6 and at the primary collimators at IR7 as illustrated in Figure 1.15 [24].

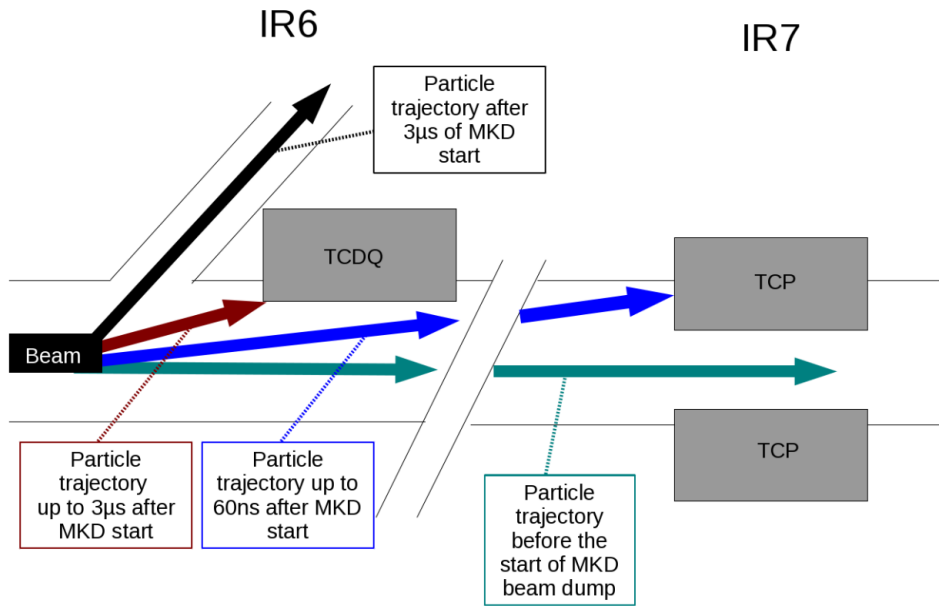


**Figure 1.15:** Illustration of beam trajectories during beam dump kicker magnet (MKD) rise time [24].

## 1.4 Simulation of high current electron beam

**Different approaches.** Beam simulations are essential to provide predictions for many beam applications. The simulations are now much more accessible thanks to the high computation power of modern computers.

High current electron beams, as for the HEL, act as non-neutral plasmas, for which there are two general descriptions: kinetic and fluid description. The core of a fluid simulation is the numerical solution of magneto-hydrodynamic equations describing the beam as a whole (fluid), while kinetic simulations take into account particle interactions via their electromagnetic field. The kinetic approach can be carried out either by solving numerically Vlasov equations, or with particle simulations, with discrete time steps, following the motion of a charged particle system for each time-step according to the particle's interactions with each other and with external fields [29].

**Particle in Cell simulations.** The computational resources needed to simulate the motion of each particle in the beam are very high. However, a system with a reduced number of simulated macro-particles, where each macro-particle is representing a larger number of real particles, can reproduce the collective behavior of the original system.

The particle-in-cell (PIC) simulations use such a principle. Each macro-particle corresponds to  $\approx 10^3$  or even  $10^6$  real particles, both macro-particle and real particles, move the same way due to the dependency of Lorentz force on the charge-to-mass ratio. Despite the usage of macro-particles, the

number of simulated particles is often still large ( $>10^5$ ) leading to a high computational load even for large clusters in some cases.

Each macro-particle carries properties such as position, velocity, charge content, etc. However, the electric field is numerically solved on a discrete mesh storing the quantities such as charge density or the calculated electrostatic self-field. Interpolation from the macro-particles to the mesh points is called particle weighting. Similarly, to calculate applied force at macro-particle from the field on the mesh, the field must be interpolated to macro-particle position, which is called field weighting [29, 30].

### 1.4.1 Warp Code Framework for Kinetic Simulations of Particle Beams and Plasmas

The Warp suite of simulation codes was originally developed for PIC simulations of space-charge dominated ion beams in accelerators [31]. Therefore, Warp uses PIC simulations and traditional accelerator codes. The space-charge forces in the high current beam dominate over the thermal forces as well as magnetic self-fields for low velocities. For that reason, the Warp uses the electrostatic particle-in-cell method where only Poisson equation is solved instead of the whole set of Maxwell equations [30, 32].

**Warp calculation.** Electrostatic potential and a charge density are discretized and saved on a mesh. The simulation repeats the following pattern for each time-step [33]:

1. The charge density is interpolated onto the mesh from the macro-particles, using linear weighting.
2. The electrostatic potential is calculated from the charge density by solving Poisson's equation.
3. The electric fields are interpolated from the mesh to the macro-particles' positions, using linear weighting.
4. The velocities and positions of the macro-particles are advanced using the "leapfrog" method.

*Particle weighting.* The charge density on the mesh points is linearly interpolated from the macro-particles. For one-dimension case the calculations are following [30]:

$$q_j = q_i \left( \frac{x_{j+1} - x_i}{\Delta x} \right), \quad q_{j+1} = q_i \left( \frac{x_i - x_j}{\Delta x} \right), \quad (1.2)$$

where  $q_j$  is linearly interpolated charge at the mesh point  $j$ , the  $x_j$  is the position of the mesh point  $j$ , the same applies for the next mesh point  $j + 1$ , the  $q_i$  and  $x_i$  denotes the macro-particle charge and position, and  $\Delta x$  the size of a mesh cell. As it can be seen the weight is linearly proportional to the distance between the particle and adjacent mesh points.

In the case of the 2-dimensional problem, the weight is linearly proportional to the area between the particle and adjacent mesh points as shown in Figure 1.16. The equations are then [30, 32]:

$$\begin{aligned}
 q_{j,k} &= q_i \left( \frac{(\Delta x - x)(\Delta y - y)}{\Delta x \Delta y} \right), \\
 q_{j,k+1} &= q_i \left( \frac{(\Delta x - x)y}{\Delta x \Delta y} \right), \\
 q_{j+1,k} &= q_i \left( \frac{x(\Delta y - y)}{\Delta x \Delta y} \right), \\
 q_{j+1,k+1} &= q_i \left( \frac{xy}{\Delta x \Delta y} \right),
 \end{aligned}
 \tag{1.3}$$

where  $x$  and  $y$  are coordinates of the macro-particle relative to the position of a mesh point  $j, k$ , and  $\Delta x, \Delta y$  the mesh sizes. To extend to the 3-dimensions one simply has to use volume instead of an area for weighting [30].

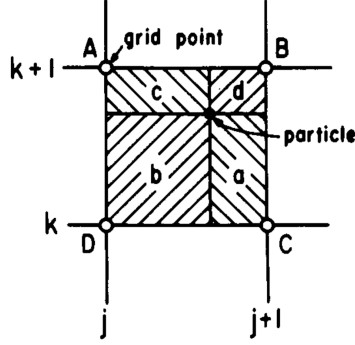


**Figure 1.16:** Scheme of linear weighting using area in 2-dimensional simulations. Areas  $a, b, c, d$  are used as weights (after normalization) corresponding to the grid point  $A, B, C, D$ , respectively. [29].

*Poisson equation.* The electrostatic potential is then numerically calculated solving Poisson equation [30]:

$$\nabla^2 \phi(x, \dots) = -\rho(x, \dots)
 \tag{1.4}$$

where  $\nabla^2 \phi$  is a laplacian (sum of second derivations) of electrostatic potential and  $\rho$  the charge density.

Warp allows to choose from several methods to solve this equation, including combination of Fast Fourier Transformation (FFT) and matrix solving methods or iterative methods. Complete list can be found in [33] and more detailed description of the methods in [34].

*Field weighting.* For consistency, field weighting, i.e. interpolation of fields from mesh points to macro-particles positions, must be the same as particle weighting. Otherwise, the resultant forces would be non-physical by creation of a self-force. Therefore, the electrostatic field at the position of

each macro-particle is linearly interpolated from surrounding 4 and 8 points in the case of 2-dimensional and 3-dimensional simulation, respectively. In the same way as for the particle weighting, the areas denoted  $a, b, c, d$  in Figure 1.16 are used as weights in case of 2-dimensional simulation. In the case of 3-dimensions, one extends the areas to volumes.

*Macro-particle advancing.* The macro-particles' position and velocity are advanced using the "leap-frog" method. This method solves finite-difference equations which approximate the first-order differential equation of motion [29]:

$$\begin{aligned} m \frac{d\vec{v}}{dt} = \vec{F} &\Rightarrow m \frac{\vec{v}_{new} - \vec{v}_{old}}{\Delta t} = \vec{F}_{old} \\ \frac{d\vec{x}}{dt} = \vec{v} &\Rightarrow \frac{\vec{x}_{new} - \vec{x}_{old}}{\Delta t} = \vec{v}_{new} \end{aligned} \quad (1.5)$$

Leap-frog method uses time discretization of macro-particle motion. For that reason, this method introduces errors proportional to the time-step size squared. Advantage of this method is that it requires low resources as it does not need to access or store any data of macro-particles at previous time-steps. It is, therefore, a fast and accurate method if the time-step is chosen small enough.

As shown in Figure 1.17 the velocities are known at half-integers and the positions at integers of time-step. Therefore, initial conditions of velocity and position given at the same time  $t = 0$ , must be changed to fit the time schemes, as detailed in [29].

An "asynchronous leap-frog" method is used, whenever user accesses the macro-particles properties i.e. when diagnostics are made. This method synchronize the velocity and position after a macro-particle advance by splitting the velocity advance so it is known at both half-integer and integer time levels, more in [35, 31]. This method is less time efficient, however, very important because with the faster leap-frog method the velocity and position are never known at the same time point which can lead to erroneous diagnostics.

**Warped coordinates.** The name *Warp* comes from Warp's ability to utilize warped Cartesian Frenet–Serret coordinates. The warped coordinates can be visualized as Cartesian coordinates in a straight section and Polar coordinates in a bend section of a simulation as illustrated in Figure 1.18 a). Mesh of the simulation then follows the center-line and is *warped* (bent).

When a warped mesh is used the number of mesh points is reduced while maintaining the precision compared to a rectangular mesh where redundant mesh points are created and calculated outside of the pipe. This allows Warp to increase the resolution and effectively simulate the space-charge effects in bent accelerator lattices [31].

*Bent-beam algorithm.* The warped coordinates can be treated as a sequence of rotated Cartesian coordinates aligned with the tangent of the bend. An exact method to calculate the particle properties in such coordinates exists,

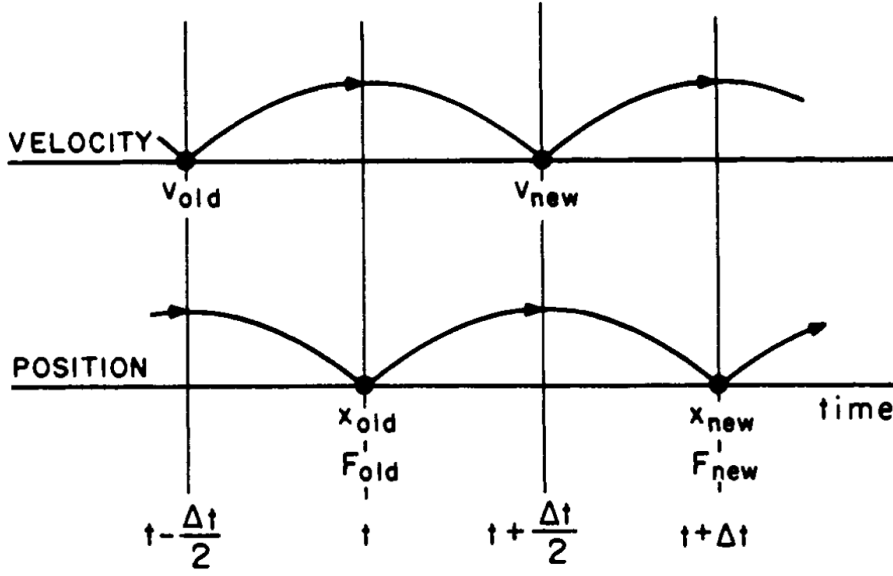


Figure 1.17: Time evolution of leap-frog algorithm [29].

however, the number of operations required is non-negligible. In Warp an approximated, fast and sufficiently accurate algorithm is implemented [37].

The implemented method translates the velocity rotation of coordinate transformation into a dipole field as a "pseudo-gyrofrequency" according to[36]:

$$B_{modif.} = B_{orig.} - \frac{m}{q} \frac{v_z}{r_* + x}, \quad (1.6)$$

where  $B_{modif.}$  is the modified implemented magnetic field,  $B_{orig.}$  original field in the bend,  $r_*$  bend radius,  $m$  mass of the particle,  $q$  its charge,  $v_z = r\dot{\theta}$  its axial speed,  $\theta$  its angle coordinate in the bend,  $x = r - r_*$  its transverse coordinate (relative to the center-line) and  $r$  its distance from the bend center as illustrated in the Figure 1.18 b).

The particle axial position is then advanced according to[36]:

$$\frac{ds}{dt} = -r_*\dot{\theta} = \frac{r_*}{r}v_z, \quad (1.7)$$

where  $s$  is the axial coordinate identical with  $z$  in straight section, but in the bend section of a simulation  $s = -r_*\theta$ .

This algorithm is inexact because it approximates the  $v_z$  and  $x$  to be constant during a time-step [37].

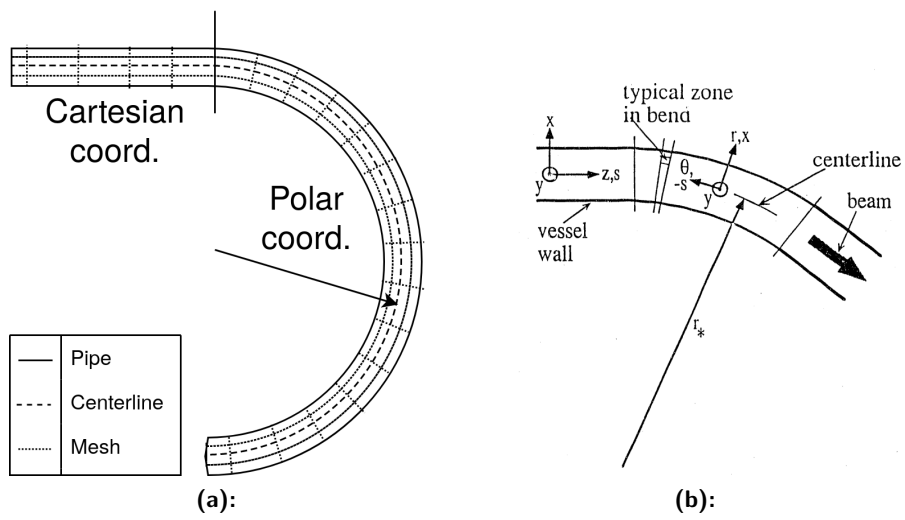


**Figure 1.18:** a) Illustration of a mesh in warped Cartesian Frenet-Serret coordinates. b) Illustration of different sets of coordinates in the bend [36].

## Chapter 2

### Practical part

#### 2.1 Calibration of Diamond Beam Loss Monitors

The Diamond Beam Loss Monitors are used to measure beam loss at several areas around LHC with different characteristics as discussed in 1.3.1. The structure of each dBLM analog chain is therefore adapted.

However, this means that the response of each dBLM to the same external conditions can differ due to different components used or imperfections in the same ones. For example, sometime additional attenuation is needed, different or no operational amplifier is used. The Diamond Beam Loss Monitors are, therefore, calibrated to take these variations into account equalizing the dBLM responses.

This calibration will be called relative calibration as the monitors then provide only relative information about the beam loss, but no absolute values.

Additionally, taking the factory calibration of the particle detector into account, the monitors can provide the magnitude of the intensity of particles passing through the detector. And furthermore, simulations can relate the magnitude of beam loss intensity to secondary particles passing through the monitor, and therefore, obtaining information about magnitude of beam loss from the BLM response.

The factory calibration is known and taken constant, therefore calibration of the particle detector is not necessary. And the mentioned simulations are done by a specialized group and out of the scope of this thesis.

Therefore, all analog and digital chains of dBLMs at LHC and injection transfer lines were relatively calibrated as a part of this theses; the list can be found in Table 1.2.

This section firstly describes the methodology of the relative calibration and then the results are presented.

**Overview of the calibration.** The calibration is carried out by calculating and implementing a constant calibration coefficient for each monitor scaling its response. The calibration is separated into three parts; Response measurement, Analysis, and Implementation as illustrated in Figure 2.1. Response measurement subsection describes the measurement of a response of each monitor to a known signal. The measured responses are then used in

Analysis subsection to calculate the calibration coefficient for each monitor. Implementation is then described in the last subsection.

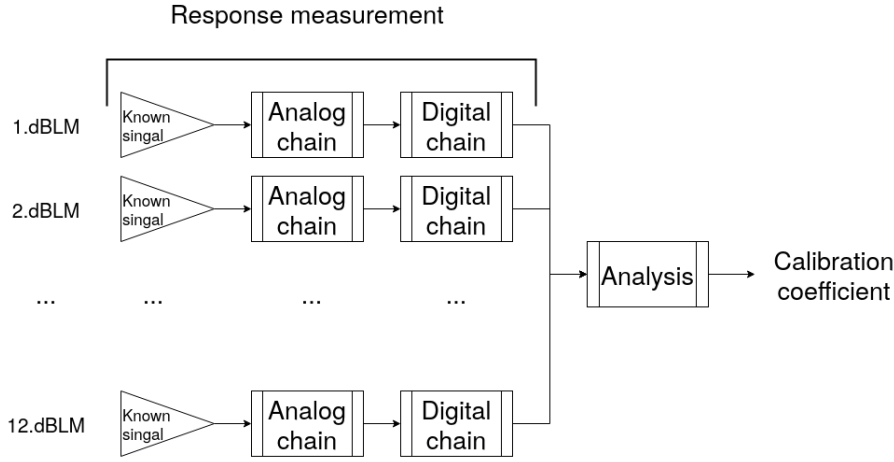


Figure 2.1: A scheme of relative diamond beam loss calibration.

### 2.1.1 Response measurement

**Measurement overview.** The measurement setup scheme is detailed in Figure 2.2. A Programmable signal generator was connected to AC/DC splitter replacing the diamond detector. The input signal was specifically designed to correspond to the detector response to registered particles. The signal then travels through an analog chain, namely AC/DC splitter, usually amplifier,  $\approx 200\text{m}$  long cable, then is digitized by ADC. The digital signal is then processed by FPGA, and the output is saved for analysis.

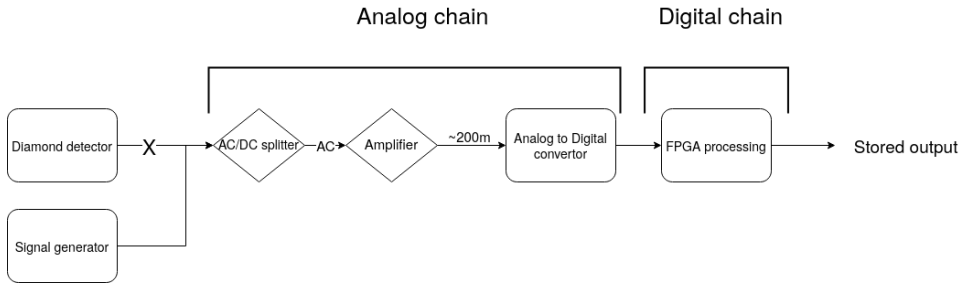


Figure 2.2: A scheme of diamond beam loss monitor response measurement.

**Input signal.** Single bunch and bunch train input waveform were used for the measurement. The single bunch waveform was composed of one signal with a repetition frequency  $1\text{MHz}$  and the train waveform consisted of 10 signals separated by  $25\text{ns}$  with repetition frequency also  $1\text{MHz}$ .

The signals in single and train waveform had the same parameters, both the positive and negative edges were set to  $1.9\text{ns}$ , with the total duration of  $3.8\text{ns}$  and baseline at  $0\text{V}$ .

The peak-to-peak amplitude of the generated signal varied according to a presence and amplification factor of the analog signal amplifier in the chain. The amplitudes for each system can be found in Table 2.1.

The signal and waveform parameters were chosen to emulate the response of the detector to the LHC bunch beam losses. An example of the train waveform (8 out of 10 signals shown) is shown in the Figure 2.3.

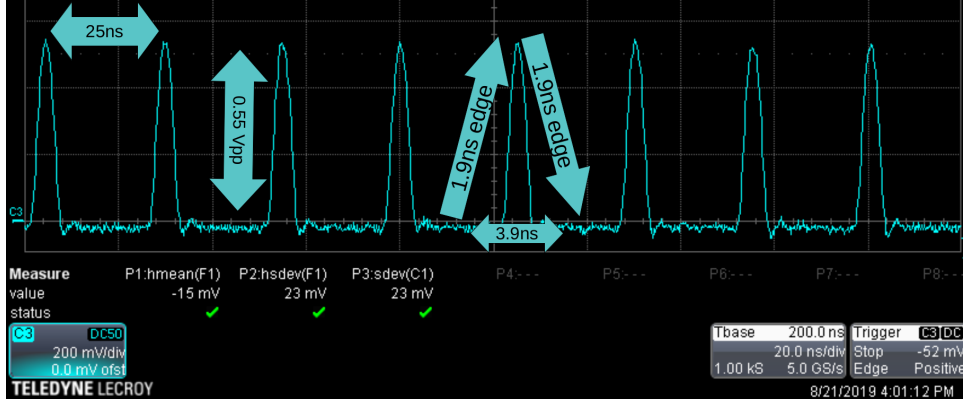


**Figure 2.3:** An example of the input train waveform (8 out of 10 signals shown). The configured signal parameters are noted, including separation between signal peaks, positive and negative edge and total signal duration. An amplitude is shown, however it changed from system to system.

**Signal generator connection to dBLM.** The signal generator was configured and then connected to the AC/DC splitter instead of the diamond detector. Identical cabling was used always to conserve the setup properties. Additional attenuation was added for setups equipped with head amplifiers. The attenuators provided up to 20 dB attenuation while the signal generator output power was kept in optimal range. The attenuation used for calibration of each system can be found in Table 2.1.

**Output storage.** The inputted signal travels through the analog chain, is digitized by a 14-bit ADC running at 650 MSPS and then is processed by an FPGA. Raw digitized data was then stored for the analysis.

## 2.1.2 Analysis

**Analysis overview.** Standard LHC beam is bunched, therefore, measured beam losses consist of peaks corresponding to these bunches as can be seen in Figure 2.4. An integral of the peak in raw data corresponds to a beam loss by a bunch. Therefore, the response of the Diamond Beam Loss Monitor is characterized, in this thesis, by averaging over integrals of the raw data corresponding to each bunch.

Relative calibration equalizes the dBLM responses (provided the same input to every monitor), as mentioned before. For that reason, calibration

coefficients are used to scale the dBLM integral and therefore relatively calibrate them when the following calibration set of equation is satisfied:

$$I_i \cdot C_i = I_j \cdot C_j, \quad (2.1)$$

for each  $i$  and  $j$  corresponding to each and every dBLM. The  $I_i$  is the average integral corresponding to the response of a dBLM  $i$  and  $C_i$  is its calibration coefficient. As can be seen, the calibration coefficients closely relate to the ratio of the dBLM responses.

Integration algorithm used to integrate raw data and which is also implemented in the data processing FPGA is described in the following paragraph. Then calibration coefficient calculation is derived from the equation 2.1 while different input signal parameters are taken into account, as described at the end of this sub section.

**Integration algorithm.** The algorithm firstly finds a peak of the signal to determine the bins to be used. The peak is defined by two consecutive rising bins followed by one bin decreasing while the difference between the last rising and fifth bin before is above a threshold. 5 bins preceding and 10 succeeding the peak are used to calculate the integral including the boundary bins, making it 16 bins in total. The baseline is estimated as an average of boundary bins, therefore, it is linearly approximated. The integration is then equal to the sum of differences between the 16 bins and baseline:

$$I = \sum_{i=-5}^{+10} (bin[i] - baseline), \quad baseline = \frac{bin[-5] + bin[10]}{2} \quad (2.2)$$

where  $i$  denotes the position of the bin relative to the peak and  $I$  is the integral.

**Calibration coefficient.** The calibration coefficient can be simply expressed from equation 2.1. However, it would require that the input signal was the same for each dBLM which was not the case as described in subsection 2.1.1. Therefore, the integral needs to be standardized to take into an account the different input signal, which can be done according to:

$$I_s = I \cdot \frac{10^{\frac{Att}{20}}}{Amp} \quad (2.3)$$

where  $I_s$  is the standardized integral,  $I$  the original integral,  $Att$  attenuation used (in dB) between the signal generator and analog chain and  $Amp$  amplitude set on the generator. Then, the calibration coefficient can be expressed as:

$$C_i = \frac{I_{ref} \cdot Amp_{ref}^{-1} \cdot 10^{\frac{Att_{ref}}{20}}}{I_i \cdot Amp_i^{-1} \cdot 10^{\frac{Att_i}{20}}}, \quad (2.4)$$

where  $ref$  refers to one dBLM chosen as a reference.

**Usage of calibration coefficient.** According to the equation 2.1, the Diamond Beam Loss Monitors can be relatively calibrated by multiplying the integral by calibration coefficient. This scaling is implemented in the FPGA as it is processing the digitized data and calculating the integrals.

dBLM tested		Generator & circuit set up par.		Output Analysis & Results	
Electronics	Ch	Att. [dB]	In Ampt. [Vpp]	Out integral [-]	Cal. coeff.[-]
ua23 TCDI:					
	0	0	5.50	2010 ± 50	41.3955
	1	20	0.55	13000 ± 200	0.0666
ua23 —:					
Inner	0	40	0.55	21300 ± 300	0.0041
Outer	1	40	0.55	21600 ± 400	0.0040
ua23 TDI:					
	0	0	1.10	170 ± 40	100.3064
	1	0	1.10	17400 ± 200	1.0000
ua87 TCDI:					
	0	0	5.50	2190 ± 40	39.6006
	1	20	0.55	12400 ± 100	0.0703
ua87 TDI:					
	0	0	1.10	160 ± 40	111.9548
	1	0	1.10	15700 ± 200	1.1073
us65 TCDQ:					
beam 1	0	20	1.10	1880 ± 50	0.9240
beam 2	1	20	1.10	1870 ± 50	0.9295
ua76 TCP.A:					
beam 1	0	40	0.55	20900 ± 300	0.0041
beam 2	1	40	0.55	19700 ± 300	0.0044
ua76 TCP.D:					
beam 1	0	40	1.10	20200 ± 300	0.0086
beam 2	1	40	1.10	23000 ± 200	0.0075
tz76 TCHS.S:					
beam 1	0	40	1.10	27200 ± 300	0.0064
beam 2	1	40	1.10	26000 ± 300	0.0067

**Table 2.1:** Summary of the relative calibration’s input parameters and average integrals of the raw output data and calculated calibration coefficients. Each Diamond Beam Loss Monitor is characterized by the detector and *Electronic* location and connected *Channel* (Ch). The generator & circuit set up parameters are: *Attenuation* (Att) at signal generator and input signal peak to peak *Amplitude* (In Ampt) of the generator. The signal input is described in subsection 2.1.1. The outputs and results are described by resulting average *Output integral* for train signal and calculated *Calibration coefficient*.

### 2.1.3 Results

Calibration coefficients were calculated and implemented for all fourteen Diamond Beam Loss Monitors at LHC and four at the injection transfer lines TI2 and TI8. The results of the calibration are described in the following paragraphs. The summary of measurement input parameters, average integral

of the output raw data and calculated calibration coefficients can be found in Table 2.1.

Several examples of single and train waveform measured output data are shown in Figure 2.4. The setup parameters for each system can be found in Table 2.1.

The bandwidth of the fast signal produced by the detector is limited mainly by the capacitance of the long cabling. This gives rise to the different shaping and increase of the width of the analog signal. Also, large differences in magnitude of the signal can be seen due to a different signal sensitivity of each monitor as expected and discussed in subsection 1.3.1.

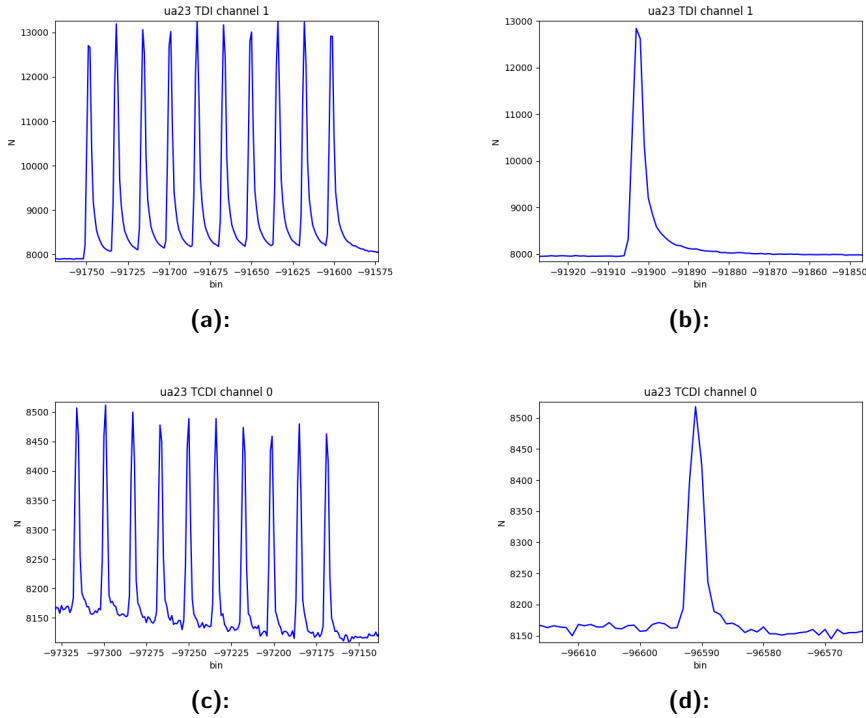


**Figure 2.4:** Measured output data of ua23 TDI channel 1 to train a), single waveform b) and ua23 TCDI channel 0 to train c), single waveform d). The setup parameters can be found in Table 2.1

A pile-up effect of  $\approx 3\%$  was observed in the response of the analog and digital system to a single bunch signal versus a 25ns spaced bunch train. Leakage of analog signal tails to the following bunch signal is responsible for a shift in baseline estimation.

The average integrals of the measurement using train waveform were used to calculate the calibration coefficients and are presented in Table 2.1.

The calibration coefficients are readied to be implemented into middleware control system of the monitors.

## 2.2 Warp simulations of Hollow Electron Lens

Warp simulations of electron beam evolution in the part of the HEL were carried out including a beam emission from 0.6-inch gun to study the evolution of a realistic beam. The focus of these simulations was to understand the details of beam transport especially in the bending of the system. Moreover, the Warp ability to use warped coordinates which can follow the bend with bent mesh allows one to compare with other simulation codes such as CST Particle Studio while reducing computational resources needed.

The simulations presented in this study are 3D electrostatic PIC simulations of the emission (from the 0.6in gun) and evolution of an electron beam in time, more about Warp simulations in section 1.4.1. The 3D simulation geometry was important to include an expected radial asymmetry caused by the system bend.

The time-step must be small enough to keep the change of the electric field of the beam small because the simulations are electrostatic. However, the simulations include the space-charge effect which is an important factor since the magnitude of the electrostatic self-field is large in comparison to the applied electric field.

The simulated geometry is according to HEL design as depicted in Figures 2.5,2.10, starting with the electron gun, including the valve, bend and junction of HEL injection arm and LHC beam pipe and ending approx. 30cm in the first main solenoid.

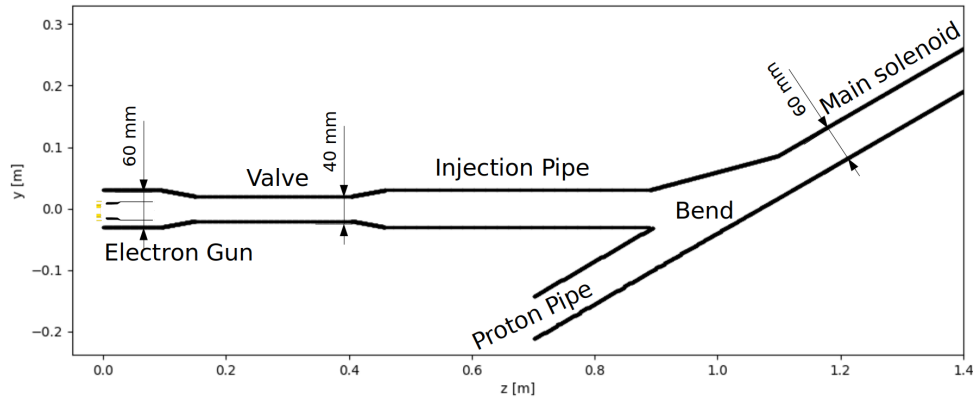


**Figure 2.5:** Longitudinal view of the simulated geometry with key parameters included. Conductors (black) are according to Hollow Electron Lens design. The electron gun is scaled design of V. Moens [38].

Computational load rises quickly with better precision, therefore, two main types of simulations were run. Heavier simulations with mesh cell size of 1.25 mm and macro-particle weight  $\approx 10^3$  were run on a workstation with 128 GB of RAM and 40 CPU threads for typically 10-40 hours to simulate 63ns of beam evolution. Lighter simulations with mesh cell size of 2.5 mm and macro-particle weight  $\approx 10^4$  were run on a laptop with 16 GB of RAM and 16 CPU threads for typically 1-20 hours again to simulate 63ns of beam

evolution.

In this section firstly the structure of the simulation code used is detailed with typical parameters mentioned. Later, the methods used to construct the conductors and remapping of the magnetic field are discussed. Then diagnostics is briefly mentioned and finally, results of the simulations are presented.

**Structure of simulation code.** The code used for the simulations will be made public with a manual at <https://gitlab.cern.ch/osedlace/warp-simulations-of-hollow-electron-lens.git>. Furthermore, the simulation code can be structured into:

- General simulation setup
  - Injection
  - Mesh setup
  - Field solver
- Magnetic field
- Conductor calculation and installation
- Diagnostics

### ■ 2.2.1 General simulation setup

**Simulation geometry.** The simulation ran for this thesis were set to be 3-dimensional. It would also be possible to use a radially symmetric geometry by changing the content of `g_sim_geometry` variable from "XYZ" to "RZ".

**Beam injection.** Beam injection was set up to be space-charge limited therefore following the Child-Langmuir law from an electron gun design. This means that the beam extraction and gun perveance is calculated from the gun mechanical design and the applied voltage between cathode and anode. The electron acceleration voltage is determined by the difference in potential between the cathode and the vacuum pipe (grounded). The gun is a scaled-down design of Vince Moens 1-in electron gun [38] to 0.6-in electron gun shown in Figure 2.6.

The maximum number of particles is set by a variable (`g_npart`), from this value the simulation code calculates a macro-particle weight. The typical weight of the macro-particle was in the order of  $10^3$  or  $10^4$  of real particles per macro-particle. However, the exact number of macro-particles and their weight is calculated according to beam extraction.

**Mesh.** The mesh cell size was typically 1.25mm for workstation simulations and 2.5mm for laptop simulations and stored in variable `g_mesh_cellsPercm` as a number of cells per centimeter. Warped coordinates, described in section 1.4.1 were utilized in the carried out simulations. The coordinates can be imagined as Cartesian in straight and Polar in bent section of the simulated

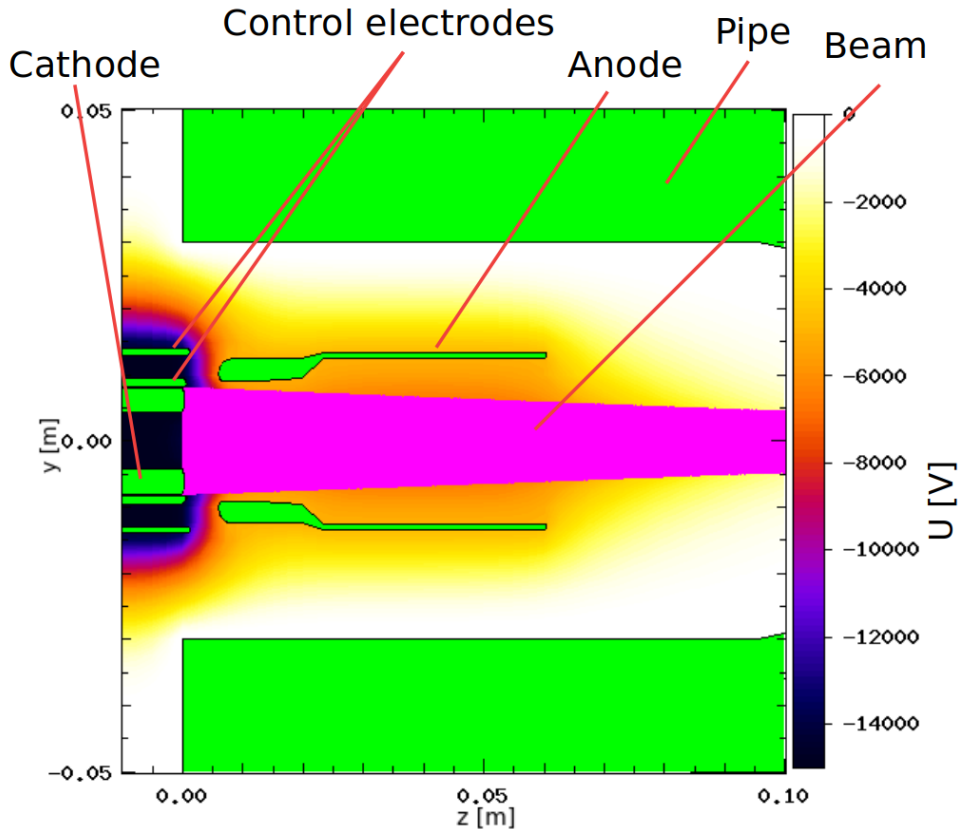


**Figure 2.6:** Longitudinal view of the electron gun geometry with a magnitude of the electrostatic field shown with  $-15\text{kV}$  on the cathode (and control electrodes),  $-5\text{kV}$  on the anode and grounded pipe. Conductors (green) are according to the scaled-down design of Vince Moens 1-in electron gun [38] to 0.634-in electron gun. The compression of the extracted beam (purple) is caused by a magnetic field.

geometry. The mesh is created to be rectangular in these Warped coordinates, therefore, in laboratory frame the mesh is bent as shown in Figure 2.7, allowing it efficiently cover the simulated area.

*Study of bent mesh effect.* The bending was chosen in a way that the mesh is centered in both injection and proton pipe as is visible in Figure 2.7. The exception is a study analyzing simulations with different bending mesh radii to probe the effect of the bent mesh on the particle trajectory and profile cross-section. The radius was extended and shorted by 9% and 45%.

In this study the mesh bending radius is different, however, the overall angle of the bend remains the same to ensure that the mesh is parallel with the proton pipe after the bend. One simulation was carried out for each mesh. The mesh center-lines are shown in Figure 2.8.

**Field solver.** The beam self-field was calculated on the mesh by MultiGrid field solver. It calculates the field by solving the Poisson equation with an iterative method. Magnetic self-field is therefore neglected. Other field solvers

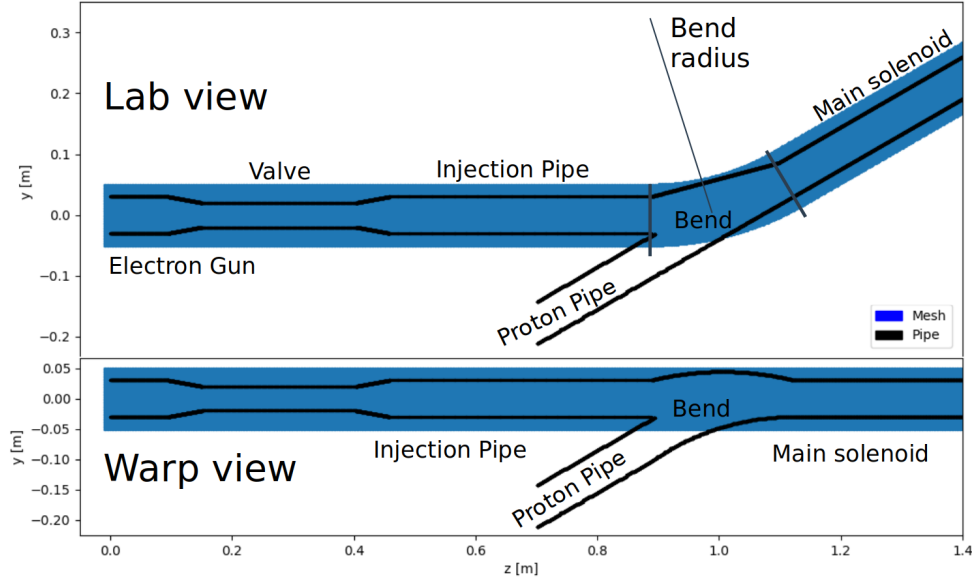


**Figure 2.7:** Longitudinal view of the mesh (blue) and conductors (black) of the simulations.

using a combination of fast Fourier transforms and matrix are available but were not used in this thesis. For more information about the field solvers see [33, 31].

**Time-step.** Time-step is an important simulation parameter because one wants it to be large enough so the number of time-steps needed to follow the beam evolution is not too high, and at the same time small enough so that all the necessary physics is taken into account. The main limiting factors are plasma frequency and cyclotron frequency. Due to the high magnetic field of 5 T in the main solenoid cyclotron frequency is several orders higher and therefore the main limitation with  $\omega_c = 8.8 \cdot 10^{11} s^{-1}$ . To ensure that the time-step is small enough it was calculated according to:

$$dt = \frac{\pi}{2\omega_c} = 1.786 \cdot 10^{-12} s \quad (2.5)$$

### 2.2.2 Magnetic field

To increase the precision of the simulation a mapped applied magnetic field was imported. The imported magnetic field was calculated by CST magnetostatic simulations using a full Hollow Electron Lens design shown in Figure 2.9. Figure 2.10 shows the relevant HEL design including the magnets used in the CST simulations.

The magnetic field obtained from CST was on a rectangular mesh with 1 mm wide cells. Because the warped coordinates were used, the magnetic field was remapped on the warp mesh before importing according to a following procedure.

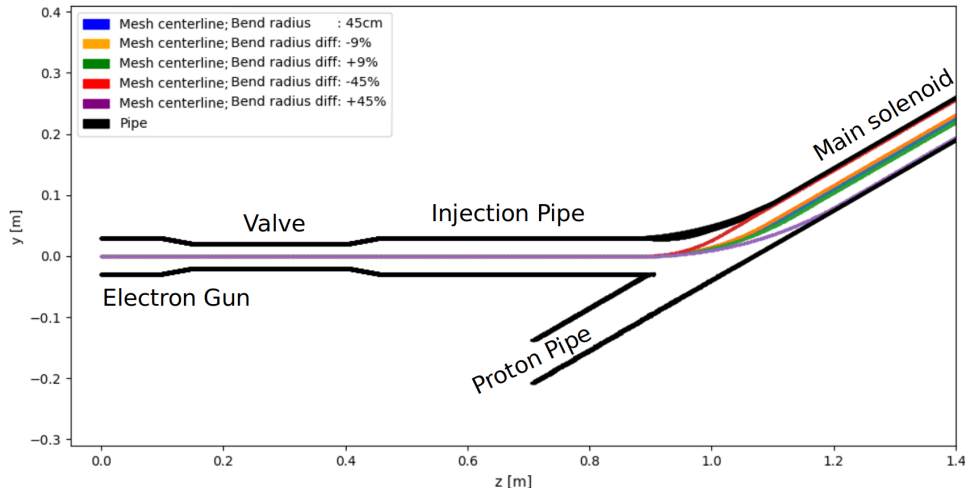


**Figure 2.8:** Longitudinal view of the mesh center-lines used in the bend effect study to probe the effect of the bent mesh on the particle trajectory and profile cross section. Each center-line represents one mesh (i.e. the blue line represent the blue column in Figure 2.7) and for each mesh one simulations was carried out.

### Magnetic field remapping.

1. Warp mesh is transformed into CST coordinate system.
2. The magnetic field at each Warp mesh point is linearly interpolated from 8 surrounding CST mesh points.
3. Warp mesh with the interpolated magnetic field is transformed from CST coordinate system into Warped coordinates.

### 2.2.3 Conductor construction

Conducting objects such as pipe and gun design were created using built-in Warp methods. Various geometric objects are available, but mostly a cylinder and surfaces of revolution were used for the installation of pipes and a for gun design. Additionally, the conductors can be joined, subtracted, or intersected allowing to create more complex geometries.

Both the injection and the LHC vacuum beam pipe at the HEL were created as a surface of revolution symmetrical around the mesh center-line. The junction between the HEL injection arm and the LHC vacuum pipe required a more complicated construction, described in the following section. To be noted that the method built in Warp will use warped coordinates for the conductors. Figure 2.11 depicts the conductors both in Warped and Cartesian (lab) coordinates.

**Junction construction.** The construction of the junction pipe can be separated into two parts, one is creating a junction and proton pipe confined by red and green lines, respectively in Figure 2.11, and the second part consist of modifying them and then joining these two conductors.

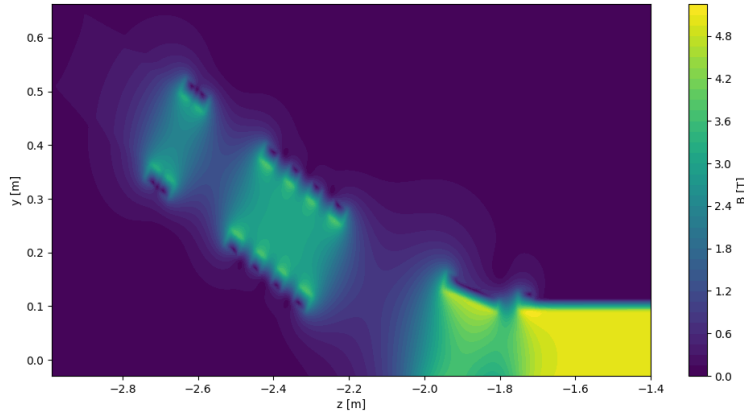


**Figure 2.9:** Magnitude of magnetic field extracted from CST and used in the Warp simulations.

*Construction of junction and proton pipe.* The pipes are created in the warped coordinate system, however one wishes to create the design in the laboratory frame. For this reason, both pipes are created according to the following procedure.

1. A pipe is defined by 4 points: The vertically highest and lowest point at the starting and ending base of the pipe in the laboratory frame.
2. A rim of the pipe is linearly discretized into a chosen number of sections
3. The parameters of every rim section are transformed from laboratory into the warped coordinate system
4. Each rim section is approximated by a cylinder parallel to the warped longitudinal axis calculated from the transformed parameters
5. Every section cylinder is added together to create the desired pipe

*Joining HEL and LHC pipe.* Before one can join the HEL bent and the LHC beam pipe both pipes must be modified as follows.

1. The inner volume of the proton pipe is subtracted from the junction pipe
2. The inner volume of the junction pipe is subtracted from the proton pipe

Then both pipes can be joined together creating the junction of injection and proton pipe outlined in Figure 2.5.

The simulations for the bend effect study had a slightly different junction pipe construction to provide better flexibility while differing the mesh. The junction pipe, in this case, was constructed as a straight pipe in the warped coordinates and therefore bent in the lab frame as is shown in Figure 2.8.

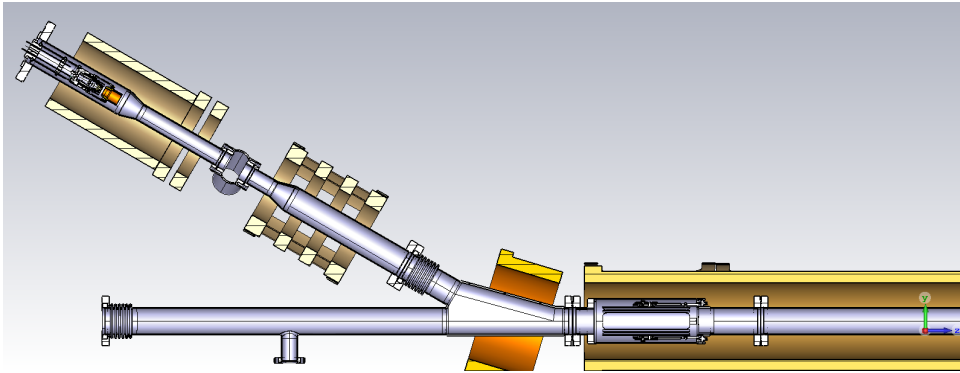


**Figure 2.10:** Hollow Electron Lens design as modeled in CST. Courtesy of Antti Kolehmainen and Diego Perini, CERN.

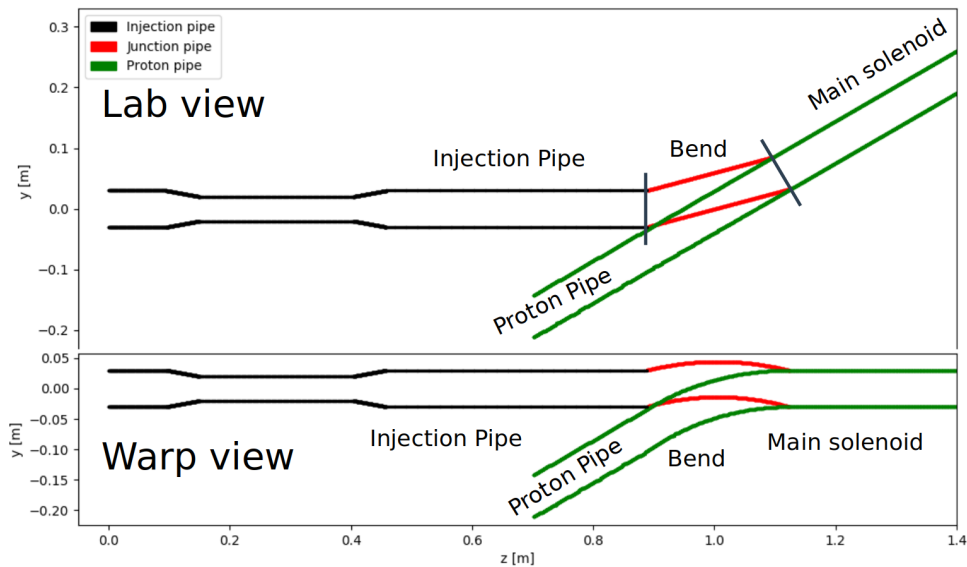


**Figure 2.11:** Injection (black), junction (red) and proton (green) pipe design to illustrate the junction construction.

## 2.2.4 Diagnostics

Two kinds of diagnostics were used, built-in warp methods, and an analysis of the data saved during the simulation.

Warp contains many built-in diagnostic tools, the one mostly used was a plotting of conductors and particle densities visualizing the beam evolution as the simulation progressed. Such diagnostics were mostly used to troubleshoot the simulations and to check basic parameters of the beam and simulation.

Warp also provides an access to the particle data and internal variables allowing them to be saved for later analysis. For this reason, the simulation configure file was saved at the start of each simulation as well as the installed conductor's geometry, imported magnetic field, mesh, and more. After the end of each simulation the position and speed of each particle was saved including the electric self-field. The size of file containing particle data is

reduced by a variable called `g_numOfDataSaved_reductionFactor` by saving only the data of every n-th particle.

### 2.2.5 Results

Numerous simulations of hollow electron beam evolution through the system were carried out to study the beam trajectory as a part of this thesis. In the following paragraphs results of these simulations are discussed. Firstly, the trajectory of the beam through the system is presented, together with the magnetic lines to verify that the beam is magnetized and follows the magnetic field lines. Secondly, the magnetic self-field is presented to justify neglecting it in the simulations. Next, the trajectory at different times is shown to check the time stability of the trajectory during the beam evolution. Then, trajectories of beams extracted with different potentials on cathode and anode are compared with each other and CST simulations. And at the end of this section, a beam simulated with meshes of different bending radii are compared to probe if the beam trajectory is affected by the usage of bent mesh.

#### Trajectory and beam magnetization

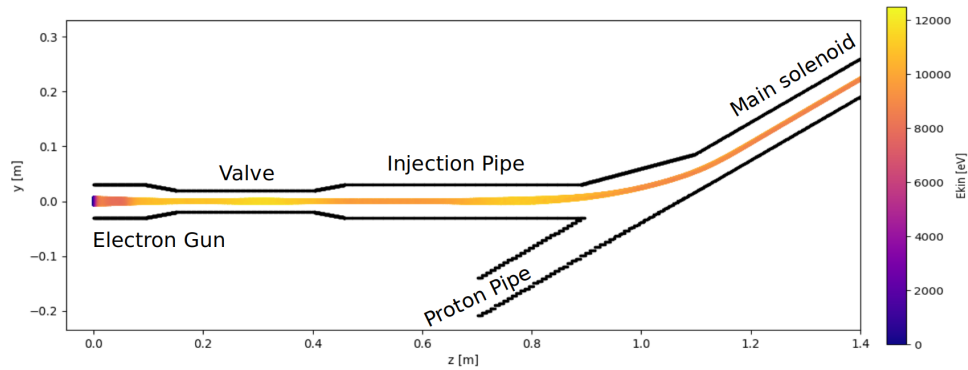


**Figure 2.12:** Longitudinal view of the beam with its energy color-coded. The potential set on the cathode was to -15kV, -5kV on anode and pipe was grounded.

A longitudinal view of a beam with its energy color-coded is shown in Figure 2.12. The presented simulation was run at the workstation, therefore, the mesh cell size was 1.25 mm, macro-particle weight  $1.0047 \cdot 10^5$ , and time-step  $1.78627 \cdot 10^{-12}$  s. A potential on the cathode was -15kV, on the anode -5kV, and the pipe was grounded.

The electron gun is immersed in a magnetic field of 0.34 T; therefore, the extracted beam should be magnetized. This means that the beam should follow the magnetic field lines and compress according to the formula for magnetic compression 1.1.

Beam trajectory is presented in Figure 2.13 in Lab and Warped coordinates where one can verify that the trajectory of the beam indeed follows the field-

lines as expected. The theoretical value of compression ratio  $\frac{r_{gun}}{r_{main}} \approx 3.67$  agrees with the calculated value from the simulations withing its error:

$$\frac{r_{gun}}{r_{main}} = 3.68 \pm 0.04mm. \quad (2.6)$$

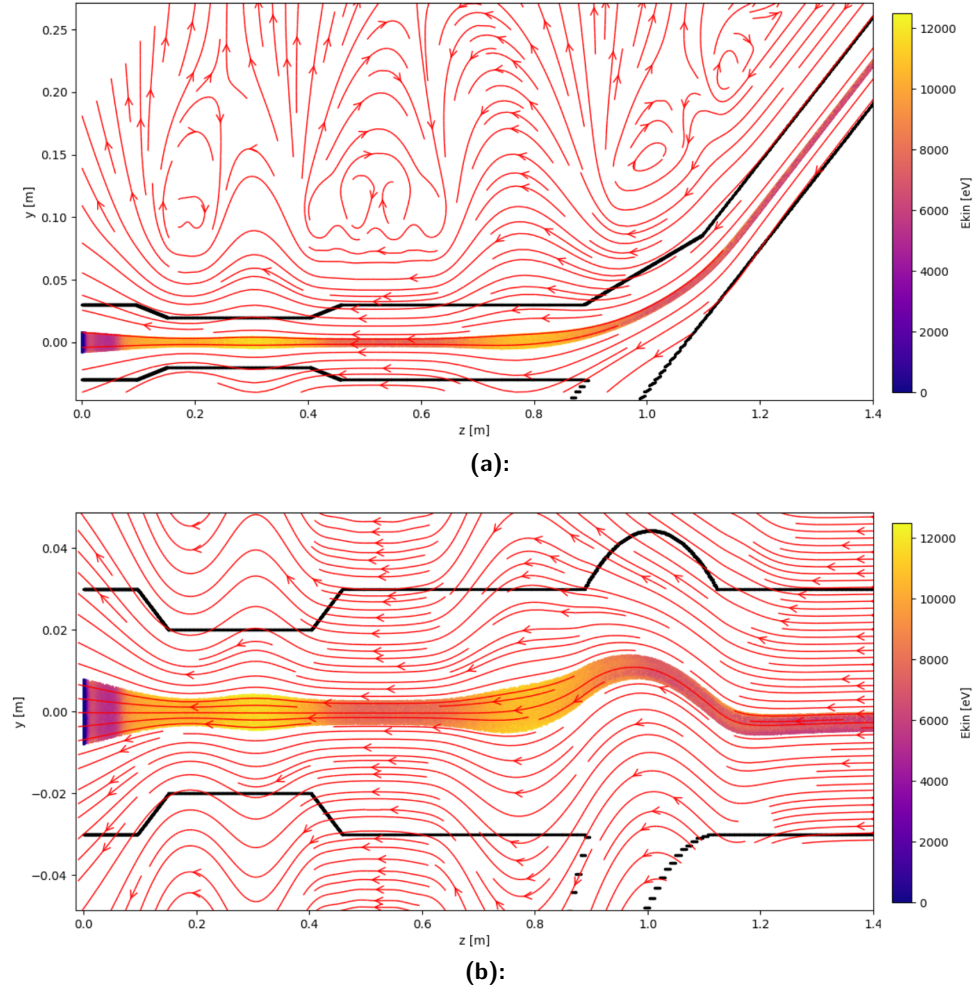


**Figure 2.13:** Longitudinal view of a beam trajectory with magnetic field lines in Cartesian a) and Warped b) coordinates. The potential on the cathode was to -15kV, on anode -5kV, and pipe was grounded.

### ■ Magnetic self-field

The magnetic self-field was not taken into account during the simulations. The magnetic self-field of the beam at 63 ns was calculated at numerous positions along the beam path. Few examples of the calculated magnetic self-field are shown in 2.14.

Neglecting the magnetic self-field in the simulations seems justified because the applied field is between 0.37 T and 5 T and the average value of the magnetic self-field amplitude is:

$$B_{amp} = 0.4 \pm 0.2 mT. \quad (2.7)$$

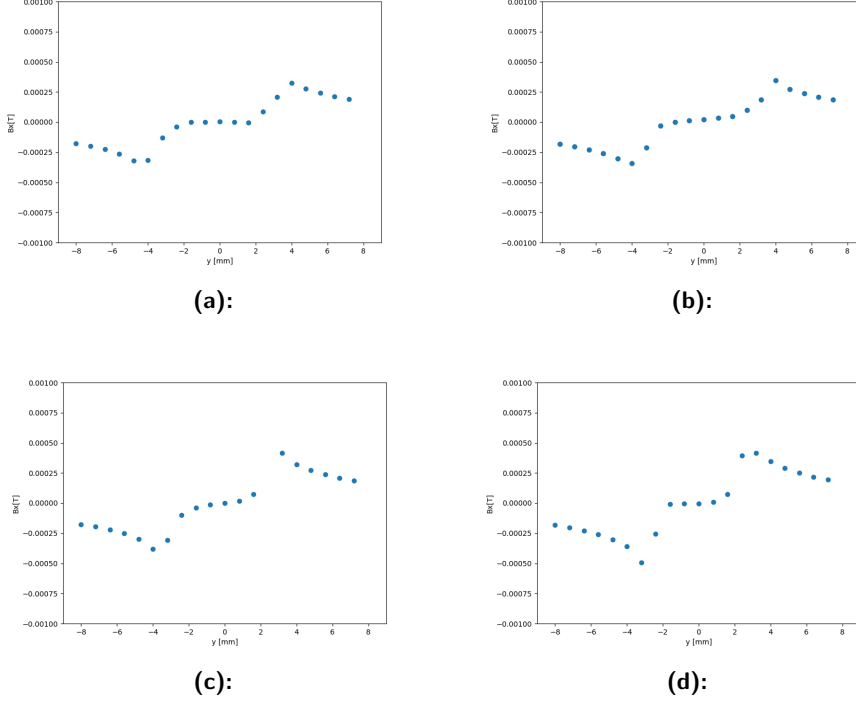


**Figure 2.14:** The calculated magnetic self-field in the beam at  $x = 0$  mm and  $z = 0.125$  m a),  $z = 0.360$  m b),  $z = 0.415$  m c),  $z = 0.525$  m d). The applied magnetic field is 0.37 T at gun and  $\approx 5$  T at the main solenoid.

### ■ Time stability

A longer beam evolution, up to 124 ns, was simulated to study the stability of the trajectory in time. The parameters of the simulations are the same as in the simulation above the only differences are that the number of time-steps completed was  $7 \cdot 10^4$  and the macro-particle weight was  $3.7 \cdot 10^4$ . A longitudinal view of the trajectories can be viewed in Figures 2.15, where it can be seen that the trajectories do not differ even after the substantial zoom.

In Figure 2.16 the average vertical beam position is shown in a frame of reference used in Figure 2.15 and CST simulations. This frame of reference has the longitudinal coordinate parallel with the proton pipe and its origin in the center of the main solenoid.

Differences in the average vertical beam position became visible after a significant zoom. Because there is no clear pattern between the trajectories one can assume that their spread represents the accuracy of the simulations leading to  $\sigma = 37 \mu\text{m}$ .

### ■ Beam offset

In Figures 2.15 and 2.16 one can also see that after the bend the beam dives approximately 1.5 mm under the center-line of the proton pipe. This so-called beam offset was also observed in CST simulations and is relatively large compared to a beam size of  $\sigma \approx 300 \mu\text{m}$ .

Laptop simulations with different potential (-5 kV, -7 kV, -10 kV) on the anode were carried out to study the beam offset behavior at different extracted current. Characteristics of the beams and the beam offset comparison with CST is shown in Figure 2.17 and 2.18, respectively.

In Figure 2.17 it can be seen that the different potential on anode causes changes in extracted current according to Child-Langmuir law and energy of the beam.

In Figure 2.18 one can see that the differences between the beam offsets of shown beams are small with a spread of  $\sigma = 28 \mu\text{m}$ . Moreover, the results agree with CST simulations within the error range.

**Virtual cathode.** A simulation with -10 kV on cathode and grounded anode and pipe was carried out. The trajectory of the beam is shown in Figure 2.19.

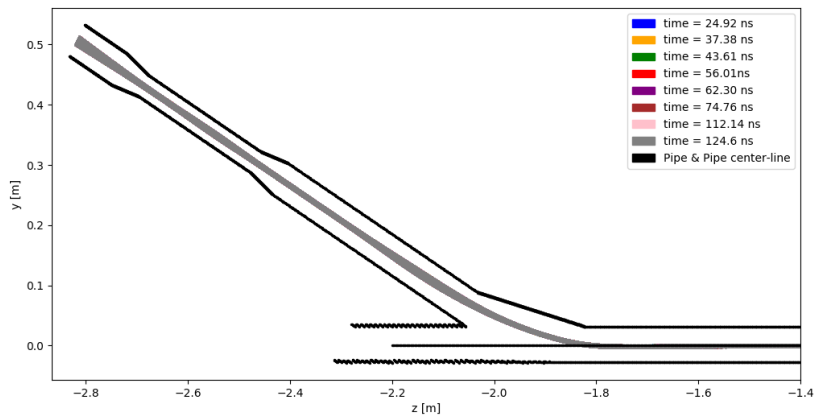
As can be seen in this simulation the electrons are slowed down during a magnetic compression to the point of a full stop and then they start to propagate in a backward direction towards the cathode. Such a phenomenon is caused by Pierce instability described in [39] and observed as well in CST simulations.

### ■ Study of mesh bending effect

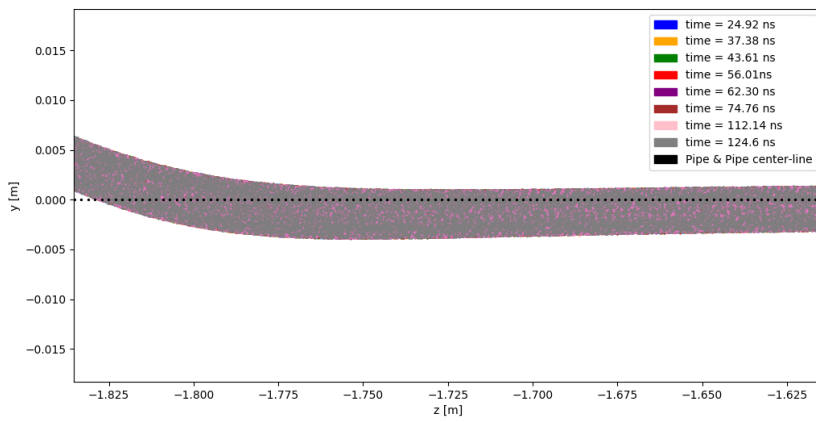
Warped coordinates were used in this thesis to bend the mesh, and therefore, reduce the number of mesh cells in the simulations. However, the warped coordinates introduce additional approximations in the bent areas as was described in section 1.4.1. Therefore, several workstation simulations with different mesh bending radii ( $\pm 9\%$  and  $\pm 45\%$ ) were carried out to probe if some artifacts are introduced into trajectory or beam profile by using bent mesh. The meshes with different radii used in the simulations are described in section 2.2.1.

Figure 2.20 shows the trajectories of beam simulated with the different meshes and Figure 2.21 their beam offsets. As can be seen, no visible differences can be seen in the trajectories even after the considerable zoom. The differences in beam offset can be observed also only after zoom-in and their spread is  $\sigma = 21 \mu\text{m}$  therefore within the error estimated from the evolution time stability described above.

Figure 2.22 shows profiles of the beams after the bend. Slight asymmetries in the shape can be seen; however, no visible artifact caused by the changing mesh bending radii is observed.



(a):



(b):

**Figure 2.15:** Longitudinal view of a beam trajectories for different evolution times in a laboratory frame parallel with proton pipe. Overall view a) zoomed section after bend b). The potential on the cathode was -15kV, on anode -5kV and pipe was grounded.

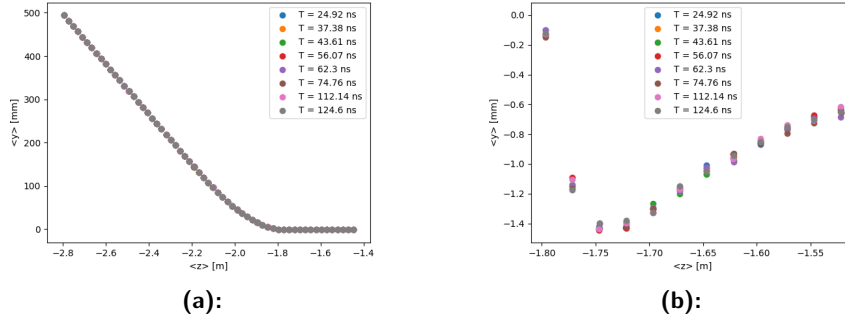


**Figure 2.16:** The average vertical beam position of a beam trajectories for different evolution times in a laboratory frame parallel with proton pipe. Overall view a) zoomed section after bend b). The spread for different evolution times is  $\sigma = 37 \mu\text{m}$ . The potential on the cathode was -15kV, on anode -5kV and pipe was grounded.

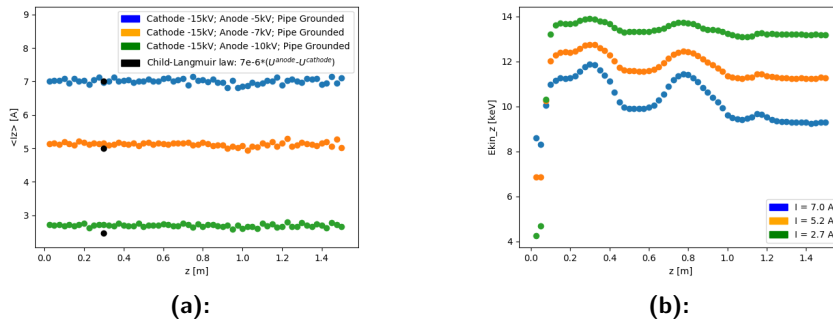


**Figure 2.17:** Current a) and Energy b) along the longitudinal warped coordinate for different anode potentials. Additionally, a current calculated from Child-Langmuir law (black) is shown for reference.

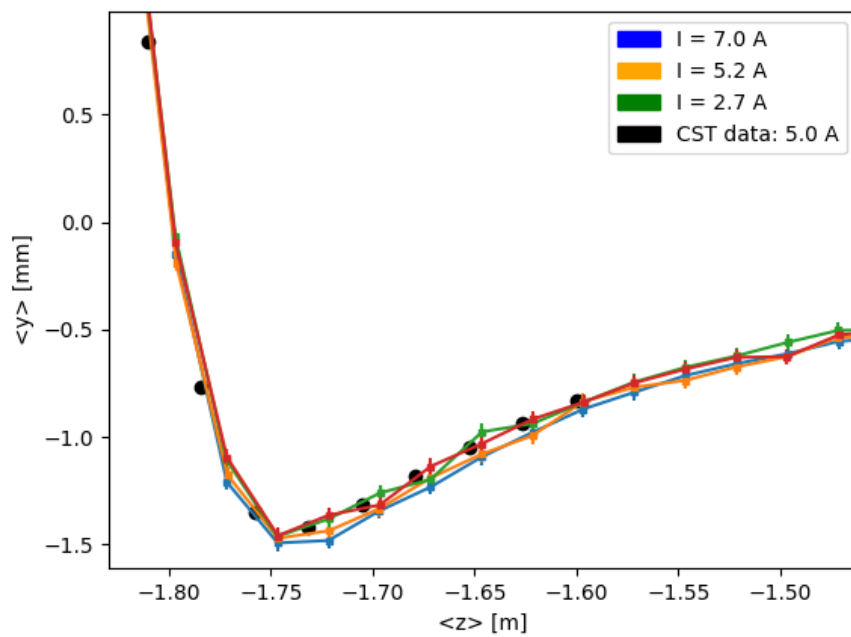
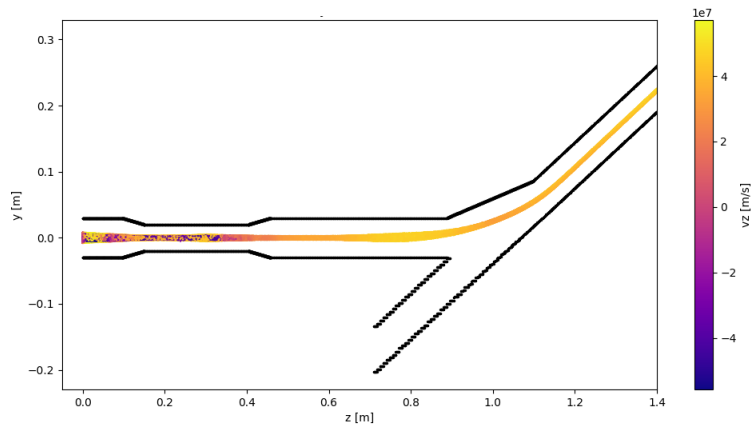
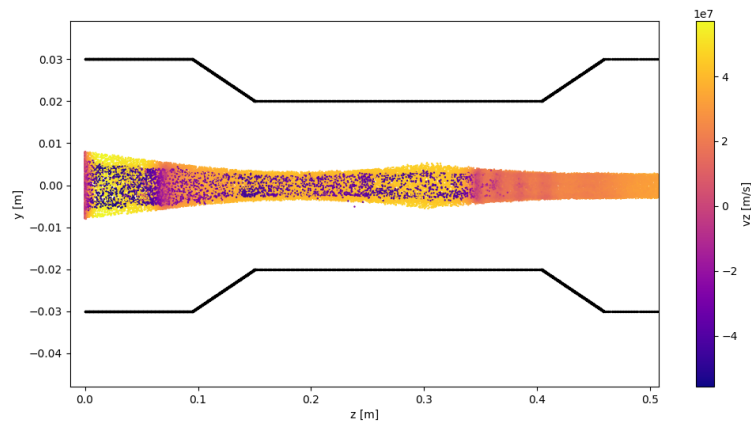


**Figure 2.18:** Beam offset behavior to varying beam current and energy and comparison to CST simulations (black). The trajectories spread for different current is  $\sigma = 28 \mu\text{m}$ . The errors presented are taken from time-stability study shown above and represent accuracy of the simulations.

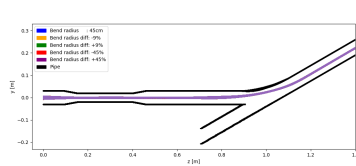


(a):

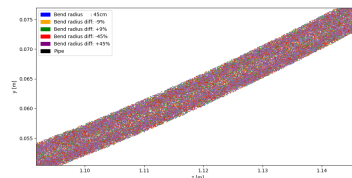


(b):

**Figure 2.19:** Longitudinal view of a beam trajectory in a laboratory frame parallel with electron pipe. Overall view a) zoomed section of the virtual cathode b). The potential on the cathode was  $-10\text{kV}$  and anode was grounded as well as the pipe.



(a):



(b):

**Figure 2.20:** Longitudinal view of a beam trajectories of simulations with different bending radii of meshes in a laboratory frame parallel with electron pipe. Overall view a) zoomed section after the bend b).

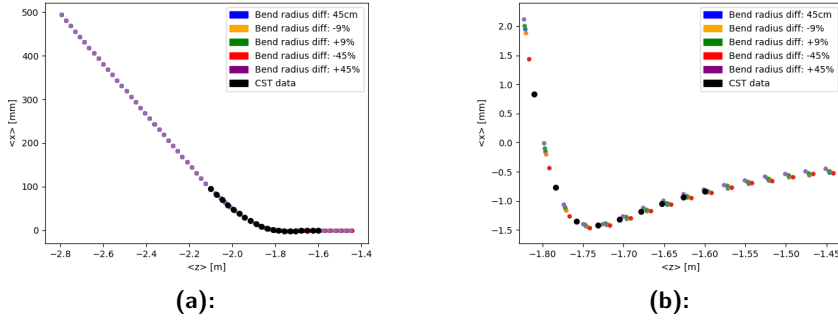


**Figure 2.21:** Beam offset of a beam trajectories of simulations with different bending radii of meshes. Overall view a) zoomed section of the virtual cathode b). The trajectories spread for different current is  $\sigma = 21 \mu\text{m}$ .

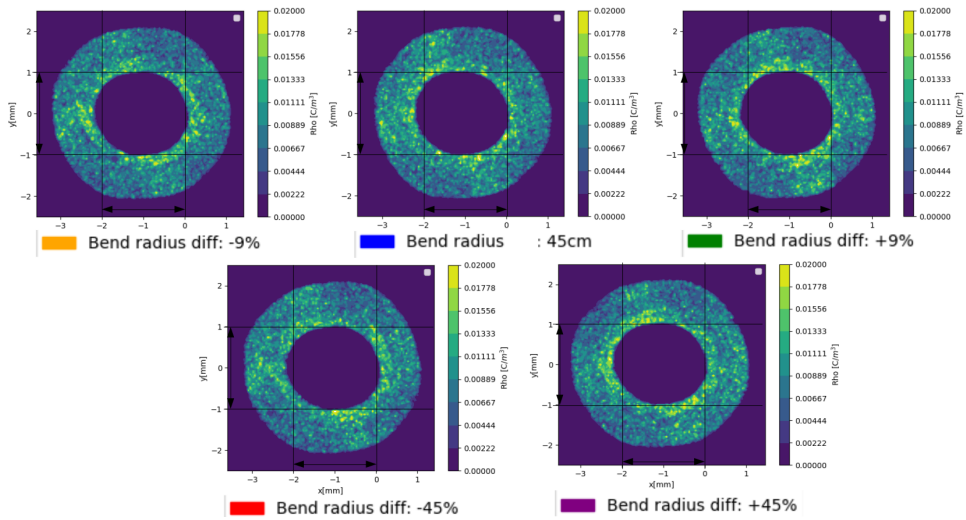


**Figure 2.22:** Beam profile of a beam trajectories of simulations with different bending radii of meshes after the bend at  $z=-1.655\text{m}$  in laboratory frame parallel with electron pipe. Slight asymmetries are visible; however, no observed artifact caused by different mesh bending radii.

## Chapter 3

### Discussion

The aim of the work described by this thesis was to produce a relative calibration of the analog and digital chain of the Diamond Beam Loss Monitors, located mostly around collimators, and simulate the trajectory of a hollow electron beam in the first half of the Hollow Electron Lens, a proposed collimation stage, using Warp code.

The dBLM calibration coefficients were calculated for every station at LHC (and its transfer lines) and are readied for implementation. The calibration is based on a measured responses of each monitor to an injected artificial LHC25ns like signal. A pile-up effect of approx. 3% was observed in the response of the analog and digital system to a single bunch signal versus a 25ns spaced bunch train. Leakage of analog signal tails to the following bunch signal is responsible for a shift in baseline estimation. Due to a low demanded precision, a correction for dBLM was not implemented in the digital chain. As a future improvement, with the data presented here, it is possible to implement a pile-up correction code. An identical correction code was implemented by the author of this thesis for a different (Fast Beam Current Measurement [40]) system, but this work is outside of the scope of the thesis.

A simulated trajectory of the hollow electron beam through the first half of HEL seems to be stable with the beam average diving  $\approx 1.5$  mm under the proton beam center-line after the bend. CST simulations of hollow electron beam trajectory in HEL also observe such beam offset after the bend and agree in comparison with Warp simulations presented in this thesis.

The beam seems to be fully magnetized and the extraction potential on anode has little to no effect on the trajectory. The spread of average beam vertical position was observed to be  $\sigma = 28 \mu\text{m}$  unless the extracted current was too high and virtual cathode was created during magnetic compression.

The beam trajectory seems to be stable in time with the spread of  $\sigma = 37 \mu\text{m}$  which represented the simulation accuracy in this thesis.

The simulations utilized so-called Warped coordinates allowing to bend the mesh, and consequently, reduce the number of mesh cells required. This method introduces some additional approximation which can potentially lead to artifacts in the simulated beam. However, a study using different mesh bending radii (up to  $\pm 45\%$ ) found no visible artifacts in the beam profile or

the trajectories which are within the simulation accuracy with a spread of the average beam positions  $\sigma = 21 \mu\text{m}$ .

The parameters of the beam in combination with the magnetic field in the simulated system keep the beam stable during its evolution. However, if more extreme beam parameters were to be simulated one should refine the time-step, the mesh cell size, and potentially also the macro-particle weight. The simulations were electrostatic, therefore the time-step needs to be small enough to keep the changes in electric self-field small. Mesh cell size can be especially important in stability studies because it can introduce asymmetries into the beam profiles (observed in this study) or affect the extracted beam distribution.



## Chapter 4

### Conclusions

Current and foreseen upgrades of the LHC rely upon improved collimation system and associated beam instrumentation. Two areas, both important parts for a collimation system upgrade, are focused in this thesis.

Firstly, Diamond Beam Loss Monitors which allow to measure and study intensive beam losses with sub-bunch precision are discussed. In this work, a method was developed and employed for a relative calibration of a digital and analog chain of every dBLM at LHC (and its transfer lines). This calibration improves the rough measure of the relative beam losses that is provided to the users. Beam loss measurements during the LHC Run 3 will profit from this calibration.

Secondly, Hollow Electron Lens which is a foreseen new advanced tool for enhancing collimation system performance as a new stage is addressed. Simulations of the hollow electron beam in the first part of the HEL using Warp code were carried out. The simulations found the trajectory of the beam to be stable, with a beam offset of  $\approx 1.5$  mm after the first bend, which is in accordance with previous CST simulations. Additionally, the simulations utilized Warp's ability to bend its mesh to reduce the computational load and increase the scalability of the simulation. A study was carried out to probe the effect of bent mesh on the beam by varying (by  $\pm 45\%$ ) mesh bending radius and found no artifacts in trajectory or beam profile caused by the mesh bending. The studies provide further improvement of the hollow electron beam trajectory understanding necessary in the HEL development.

## Appendix A

### Bibliography

- [1] Esma Mobs. The CERN accelerator complex - 2019. Complexe des accélérateurs du CERN - 2019. jul 2019.
- [2] Jean-Philippe Tock, Mateusz Bednarek, and Et.al. The second LHC long shutdown (LS2) for the superconducting magnets. In *Proceedings, 9th International Particle Accelerator Conference (IPAC 2018): Vancouver, BC Canada*, page 39, 2018.
- [3] G. Apollinari, L. Rossi, and Et.al. High Luminosity Large Hadron Collider HL-LHC. may 2017.
- [4] Wolfgang Walkowiak. ATLAS Plans for the High-Luminosity LHC. Technical Report ATL-PHYS-PROC-2018-048, CERN, Geneva, jun 2018.
- [5] Alessio Mereghetti, Stefano Redaelli, and Et.al. Collimation System Upgrades for the High Luminosity Large Hadron Collider and Expected Cleaning Performance in Run 3. In *10th Int. Partile Accelerator Conf.(IPAC'19), Melbourne, Australia, May 2019*. JACOW Publishing, Geneva, Switzerland, 2019.
- [6] A Mereghetti, S Redaelli, G Stancari, and Et.al. Hollow electron-lens assisted collimation and plans for the LHC. (FERMILAB-CONF-18-311-AD-APC), 2018.
- [7] S Redaelli. Beam Cleaning and Collimation Systems, 2016.
- [8] Oliver Sim Brüning, Paul Collier, and Et.al. *LHC Design Report*. CERN Yellow Reports: Monographs. CERN, Geneva, 2004.
- [9] D. Perini, G. Gobbi, and Et.al. The development programme of cathodes and electron guns for the Hollow Electron Lenses of the High Luminosity LHC project. *Journal of Physics: Conference Series*, 2019.
- [10] Giulio Stancari, Stefano Redaelli, Adriana Rossi, and Et.al. Conceptual design of hollow electron lenses for beam halo control in the Large Hadron Collider. Technical Report FERMILAB-TM-2572-APC. FERMILAB-TM-2572-APC, CERN, 2014.

- [11] Stefano Redaelli, A Rossi, G Stancari, and Et.al. Plans for deployment of hollow electron lenses at the LHC for enhanced beam collimation. Technical report, 2015.
- [12] Gianluca Valentino and Et.al. What did we learn about halo population during MDs and regular operation? *Review of the needs for a hollow e-lens for the HL-LHC*, 2016.
- [13] Giulio Stancari, A Valishev, G Annala, and Et.al. Collimation with hollow electron beams. *Physical Review Letters*, 107(8):84802, 2011.
- [14] V Shiltsev, Yu Alexahin, Kip Bishofberger, and Et.al. Experimental studies of compensation of beam–beam effects with Tevatron electron lenses. *New Journal of Physics*, 10(4):43042, 2008.
- [15] G Stancari, G Annala, and Et.al. Measurements of transverse beam diffusion rates in the Fermilab Tevatron collider. Technical report, Fermi National Accelerator Lab.(FNAL), Batavia, IL (United States), 2011.
- [16] M. Gasior, R. Jones, T. Lefevre, and Et.al. Introduction to Beam Instrumentation and Diagnostics. *Proceedings of the CAS-CERN Accelerator School: Advanced Accelerator Physics*, 2016.
- [17] Eva Barbara Holzer, Christos Zamantzas, and Et.al. Beam loss monitoring system for the LHC. In *IEEE Nuclear Science Symposium Conference Record*, volume 2, pages 1052–1056, 2005.
- [18] Kay Wittenburg. Beam loss monitoring and control. In *Proceedings of EPAC*, pages 109–113, 2002.
- [19] Peter Strehl. *Beam instrumentation and diagnostics*. Springer, 2006.
- [20] A Zhukov and Et.al. Beam loss monitors: physics, simulations and applications in accelerators. In *Beam Instrumentation Workshop*, 2010.
- [21] George G Guilbault. *Practical fluorescence*, volume 3. CRC Press, 1990.
- [22] B. Dehning, E. Effinger, C. Zamantzas, and Et.al. The LHC beam loss measurement system. In *Proceedings of the IEEE Particle Accelerator Conference*, pages 4192–4194, 2007.
- [23] Dmitry Gudkov, Viatcheslav Grishin, Christos Zamantzas, and Et.al. Construction of a Mobile Irradiation Instrument for the Verification of the CERN LHC Beam Loss Monitoring System. 2018.
- [24] M Hempel, T Baer, W Lohmann, and Et.al. Bunch-by-Bunch Beam Loss Diagnostics with Diamond Detectors at the LHC. *HB2012, Beijing, September*, 2012.
- [25] Chen Xu, Bernd Dehning, Erich Griesmayer, and Et.al. Diamond Monitor Based Beam Loss Measurements in the LHC. In *Proceedings, 5th International Beam Instrumentation Conference (IBIC 2016): Barcelona, Spain, September 11-15, 2016*, 2017.

